The Astrophysical Journal, 895:125 (13pp), 2020 June 1 https://doi.org/10.3847/1538-4357/ab557a

A Microlensing Accretion Disk Size Measurement in the Lensed Quasar WFI 2026–4536

Matthew A. Cornachione[1], Christopher W. Morgan[1], Martin Millon[2], Misty C. Bentz[3], Frederic Courbin[2], Vivien Bonvin[2], and Emilio E. Falco[4]
[1] Department of Physics, United States Naval Academy, 572C Holloway Rd., Annapolis, MD 21402, USA; cornachi@usna.edu
[2] Institute of Physics, Laboratoire d' Astrophysique, École Polytechnique Fédérale de Lausanne (EPFL), Observatoire de Sauverny, 1290 Versoix, Switzerland
[3] Department of Physics and Astronomy, Georgia State University, Atlanta, GA 30303, USA; bentz@astro.gsu.edu
[4] Harvard–Smithsonian Center for Astrophysics, 60 Garden St., Cambridge, MA 02138, USA
Received 2019 April 24; revised 2019 November 6; accepted 2019 November 6; published 2020 June 4

Abstract

We use 13 seasons of *R*-band photometry from the 1.2 m Leonard Euler Swiss Telescope at La Silla to examine microlensing variability in the quadruply imaged lensed quasar WFI 2026–4536. The lightcurves exhibit ∼0.2 mag of uncorrelated variability across all epochs and a prominent single feature of ∼0.1 mag within a single season. We analyze this variability to constrain the size of the quasar's accretion disk. Adopting a nominal inclination of 60°, we find an accretion disk scale radius of $\log(r_s/\mathrm{cm}) = 15.74^{+0.34}_{-0.29}$ at a rest-frame wavelength of 2043 Å, and we estimate a black hole mass of $\log(M_{\mathrm{BH}}/M_{\odot}) = 9.18^{+0.39}_{-0.34}$, based on the C IV line in VLT spectra. This size measurement is fully consistent with the quasar accretion disk size—black hole mass relation, providing another system in which the accretion disk is larger than predicted by thin-disk theory.

Unified Astronomy Thesaurus concepts: Quasar microlensing (1318); Gravitational microlensing (672); Strong gravitational lensing (1643); Reverberation mapping (2019)

1. Introduction

Quasars, a class of active galactic nuclei (AGNs; e.g., Antonucci 1993; Urry & Padovani 1995), have been an area of intense study for decades. However, their small physical sizes subtend angles that are much smaller than the resolution limit of any existing telescope. Hence, we have been forced to infer the physics powering these luminous sources by studying intrinsic flux variability (e.g., Vanden Berk et al. 2004; Sergeev et al. 2005; Cackett et al. 2007; Kelly et al. 2009; MacLeod et al. 2010), modeling spectral profiles (Sun & Malkan 1989; Bonning et al. 2007; Gaskell 2008; Hall et al. 2018), or using reverberation mapping (e.g., Peterson et al. 2004; Bentz et al. 2010; Edelson et al. 2015; Cackett et al. 2018). While these methods have provided insights into quasar structure and central black hole masses, the accretion disk continuum size and temperature profile remain open research areas.

Microlensing, first observed by Chang & Refsdal (1979), has offered an opportunity to better measure the size of quasars. Strongly lensed quasar images are magnified by a complex field of stellar-mass objects in the lens galaxy. As the quasar moves relative to our line of sight, the magnification changes, generating significant uncorrelated variability between images on timescales of months to years. If the time delays between images are known, it is possible to distinguish the correlated instrinsic quasar variability from the uncorrelated microlensing variability. Kochanek (2004) developed a Bayesian Monte Carlo technique to measure the sizes of quasars from multiple-epoch lightcurves. With this technique, we have made measurements of accretion disk scale sizes in 15 quasars (Kochanek et al. 2006; Morgan et al. 2006, 2008, 2010, 2012, 2018; Poindexter et al. 2007; Hainline et al. 2012, 2013; Mosquera et al. 2013; Blackburne et al. 2014; MacLeod et al. 2015). This method requires cosmological modeling of the effective transverse velocity, but is insensitive to uncertainty in the median mass of stars in the lens galaxy. A machine learning analysis technique, developed by Vernardos & Tsagkatakis (2019), may allow for more rapid analysis of larger sets of quasar lightcurves.

Alternatively, microlensing sizes can be inferred from chromatic variation between lensed images. In this method a quasar is imaged at a single-epoch across multiple filter bands. This approach has generated complementary measurements of quasar accretion disk sizes (Pooley et al. 2007; Bate et al. 2008; Blackburne et al. 2011; Mediavilla et al. 2011; Mosquera et al. 2011; Pooley et al. 2012; Jiménez-Vicente et al. 2012; Schechter et al. 2014; Motta et al. 2017; Bate et al. 2018). This method uses dramatically less observing time, but requires careful treatment of broad emission line contamination and flux offsets due to dust or millilensing. Furthermore, all reported sizes are subject to an assumed prior on the unknown median mass of stars in the lens galaxy. Nevertheless, when combined with constraints from multi-epoch studies, the single-epoch method generally gives similar accretion disk size measurements.

Because of the rarity of lensed quasar discoveries and the onerous observing requirements of multi-epoch studies, only 14 multi-epoch size measurements have been reported to date (Morgan et al. 2018, and references therein). Here we increase that number to 15 with the addition of the quadruply lensed WFI J2026–4536 (hereafter WFI2026)[5] (Morgan et al. 2004). The quasar source is at redshift $z_s = 2.23$, but the lens redshift was not measurable in archival spectra from the Very Large Telescope (VLT). The lens galaxy is faint and stacked galaxy spectra from 14 exposures show no distinct spectral features. Although we were unable to estimate the lens redshift, we succeeded in using these archival VLT spectra to measure the black hole mass.

Two different investigations have already used the single-epoch technique to estimate the accretion disk size in this system. Blackburne et al. (2011) observed WFI2026 in the infrared using the Persson's Auxiliary Nasmyth Infrared Camera (PANIC) on the Baade telescope and in the optical using the Raymond and Beverly Sackler Magellan Instant Camera (MagIC) on both the

[5] Based on observations made with the ESO-VLT Unit Telescope 2 Kueyen (Cerro Paranal, Chile; Programs 074.A-0563 and 075.A-0377, PI: G. Meylan).

Clay and Baade telescopes at Las Campanas Observatory. They estimated an accretion disk half-light radius of $\log(r_{1/2}/\mathrm{cm}) = 16.46 \pm 0.32$ at 2043 Å, under a log-prior on $r_{1/2}$. A recent analysis by Bate et al. (2018) using IR and UVIS channels on the Wide Field Camera 3 (WFC3) on the Hubble Space Telescope (HST) found evidence for a smaller size, $\log(r_{1/2}/\mathrm{cm}) < 16$ (rescaled to 2043 Å from an observed 1026 Å). Both of these estimates assume a $0.3M_{\odot}$ median stellar mass in the lens galaxy.

Analysis of our 13 season lightcurve complements these previous studies with a multi-epoch constraint on the scale radius, r_s, and addresses the mild tension between previous results. Note that these studies reported the measured size as a half-light radius, $r_{1/2}$, while we cast our results as a thin-disk scale radius, $r_s = r_{1/2}/2.44$, to facilitate comparison with theoretical disk models. In any case, Mortonson et al. (2005) showed that projected area, not shape, dominates microlensing variability, so these radii are directly proportional with $r_s = r_{1/2}/a$. The scaling factor a depends on the assumed disk geometry with $a = 2.44$ for a thin disk and $a = 1.18$ for a Gaussian disk.

This paper is organized as follows. In Section 2, we present our monitoring data, photometric technique, and the reduced lightcurves. In Section 3 we present our strong lens modeling and our determination of time delays for the system. We discuss our microlensing model in Section 4, and we present our measurements for the WFI2026 disk size and black hole mass in Section 5. In Section 6 we compare our measurements to those of Blackburne et al. (2011) and Bate et al. (2018), and we conclude with a discussion of the accretion disk size and black hole mass in the context of previous multi-epoch studies.

2. Data

The observational campaign was conducted within the scope of the COSmological MOnitoring of GRAvItational Lenses (COSMOGRAIL) collaboration (e.g., Courbin et al. 2005; Bonvin et al. 2018) We used images of WFI2026 obtained with the Swiss 1.2 m Leonhard Euler telescope (hereafter Euler) located at La Silla Observatory in Chile between 2004 April and 2016 November. Prior to 2010 we collected data using the C2 chip, a 2048 × 2048 detector with a pixel scale of 0.″344. We took more recent exposures on the EulerCAM (ECAM) detector, with a smaller pixel scale of 0.″2149 and dimensions of 3496 × 3512 pixels. Across all epochs we used the Rouge Genéve (RG) filter, a modified *R*-band filter with an effective wavelength of 6600 Å. At each of the 548 epochs, we obtained five 360 s subexposures. Our observations with Euler spanned 13 seasons with a typical observation cadence of once every six days for C2 and once every four days for ECAM, with inter-season gaps of ∼100 days. In Figure 1 we show a stacked ECAM exposure of WFI2026 indicating the reference stars used for point-spread function (PSF) calibration and flux normalization (*N*).

The angular separation between images in WFI2026 is small, with a scale size of ∼1.″4 (Morgan et al. 2004; Véron-Cetty & Véron 2010), making photometric measurements challenging. Nevertheless, with a typical seeing of 1.″6 with C2 and 1.″4 with ECAM, the angular separations are above the Nyquist limit ($\approx\frac{1}{2}$ seeing = 0.″8) for most image pairs. Images B and C are separated from each other and A1 and A2 by at least 1.″0. The merging pair A1 and A2, however, is only separated by ∼0.″3, too close to resolve fluxes in the individual images. We

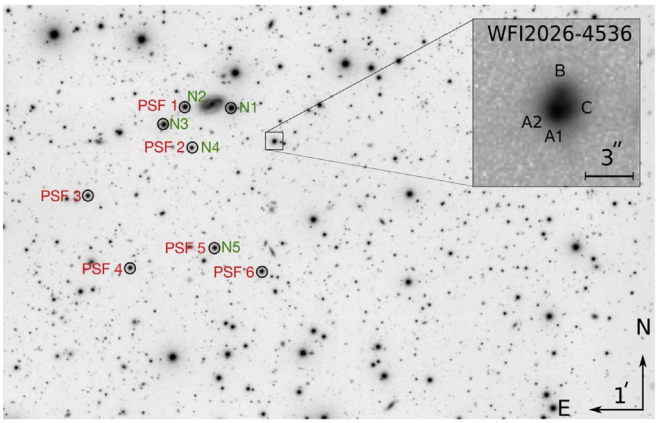

Figure 1. Deep-field stack of reduced images of WFI2026 from the ECAM detector. Stars used for fitting the point-spread function (PSF) are labeled red and stars used for flux normalization (*N*) are labeled green. The relative positions of the lensed quasar images are indicated in the expanded box, showing a single subexposure in excellent seeing.

reduced the data and performed our subsequent analysis using the combined flux A = A1+A2. We employed the Magain, Courbin, and Sohy (MCS) deconvolution algorithm of Magain et al. (1998, 2007) for deblending flux from the multiple images. Using a PSF measured from nearby reference stars, this algorithm computes a high-resolution deconvolved image of the quasar. We then followed the approach discussed in Vuissoz et al. (2007, 2008) to find flux in individual images, including priors on astrometry from Chantry et al. (2010) to further improve accuracy. We measured image fluxes in each subexposure and calculated the median value at each epoch to provide the reduced lightcurves shown in Figure 2 and in the Appendix.

The compact angular size of the system gave rise to significant cross-talk between photometric measurements. This additional noise, in excess of photon shot-noise, is typical for multiply lensed quasars. For image C in WFI2026, however, this cross-talk noise was of the same order as the intra-season variability and could mimic a microlensing signal. To mitigate this effect, we averaged over each season for image C and used these season averages in our microlensing analysis. We determined each season average for image C, $\langle c \rangle$, using least-squares fitting. The error bars, $\langle \sigma_c \rangle$, were selected such that within each season the χ^2 value, relative to the reduced lightcurve, was equal to the number of exposures, *N*, for the season. This amounted to numerically solving

$$N = \sum_i^N \frac{(c_i - \langle c \rangle)^2}{\sigma_i^2 + \langle \sigma_c \rangle^2}. \quad (1)$$

for $\langle \sigma_c \rangle$. The values c_i and σ_i came from the reduced lightcurve. This simplification removed our ability to discern intra-season variability, but allowed us to more confidently measure the annual variability, which dominates the microlensing signal in WFI2026 (Mosquera & Kochanek 2011). We show the image C season averages overlaid atop the reduced lightcurve in Figure 2.

For lens modeling we used HST imaging from the CfA-Arizona Space Telescope Survey (CASTLES[6]) (Muñoz et al. 1998; Kochanek et al. 1999; Lehár et al. 2000). Our exposure

[6] https://www.cfa.harvard.edu/castles/

Table 1
Astrometric Measurements for WFI2026 Based on HST CASTLES Imaging, F160W Band

Component	ΔR.A. (″)	ΔDecl. (″)	r_e (″)	e	θ_e (°)	F160W (mag)
A1	0.163 ± 0.003	−1.428 ± 0.003	⋯	⋯	⋯	15.64 ± 0.01
A2	0.416 ± 0.003	−1.214 ± 0.003	⋯	⋯	⋯	16.09 ± 0.01
B	≡0.000	≡0.000	⋯	⋯	⋯	17.11 ± 0.01
C	−0.572 ± 0.003	−1.042 ± 0.003	⋯	⋯	⋯	17.33 ± 0.02
G	−0.074 ± 0.012	−0.798 ± 0.008	0.47 ± 0.36	0.35 ± 0.21	53 ± 42	18.80 ± 0.43

Note. We used image B as the position reference. The lens galaxy is indicated by G. The effective radius, r_e, ellipticity, e, and position angle, θ_e, are indicated for the galaxy using a de Vaucouleurs profile.

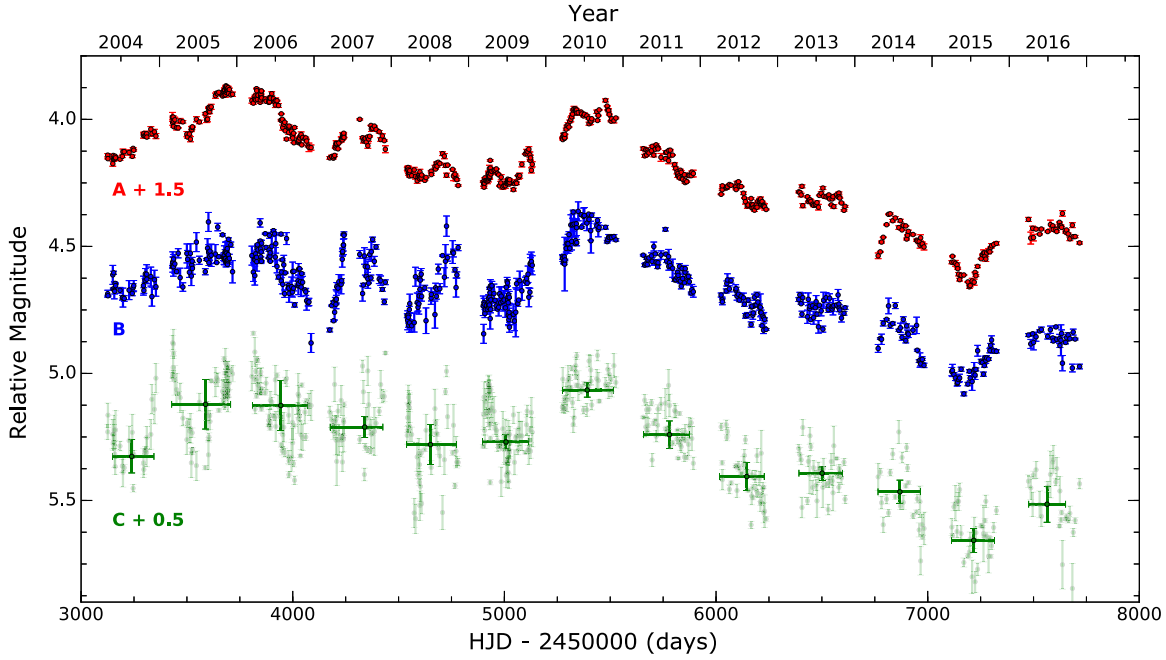

Figure 2. Reduced lightcurve for WFI2026 obtained with Euler. The curves are plotted in relative magnitudes with an arbitrary offset. Image A (A1+A2) is red, image B is blue, and image C is green. The season averages for image C are overlaid on the reduced lightcurve.

was taken on 2003 October 21 with the Near-Infrared Camera and Multi-Object Spectrograph (NICMOS) through the F160W filter (Morgan et al. 2004). From this image, we derived astrometry using the *imfitfits* routine of Lehár et al. (2000). Our astrometric fits, including the shape parameters for a de Vaucouleurs lens galaxy, are shown in Table 1. Because the lens galaxy in WFI2026 is faint, the galaxy model parameters have sizable uncertainties, but the results are in agreement with values reported in Chantry et al. (2010).

We also analyzed spectra obtained using the VLT of the European Southern Observatory (ESO) with the FORS1 mult-object spectrograph. In our analysis we use a series of fourteen 1400 s exposures through the GG435 filter obtained between 2004 and 2006. The slit was oriented to capture both images A (A1 + A2) and B. Each exposure spanned the observed wavelength range of 4400–8690 Å. For WFI2026 at $z_s = 2.23$ we fully resolved the C IV line, which allowed us to estimate the black hole mass (see Section 5.2). We display these spectra in Figure 3.

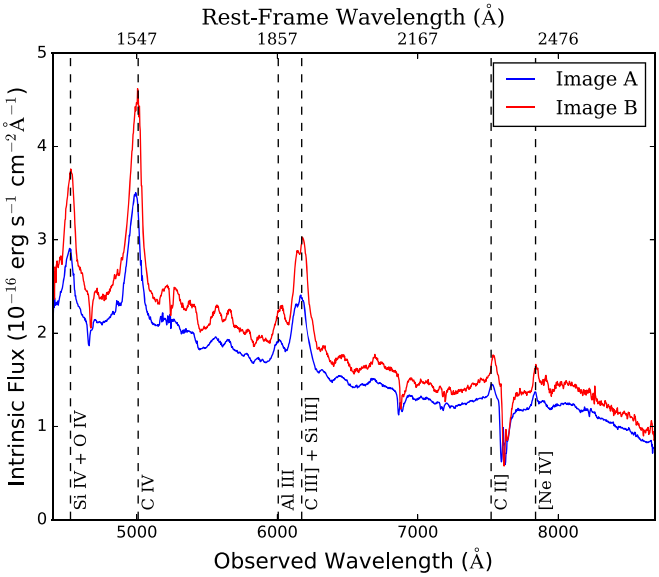

Figure 3. Reduced VLT FORS1 spectra for images A (blue) and B (red), magnification corrected to intrinsic flux estimates. The locations of several known emission lines are marked and the corresponding rest-frame wavelength is indicated along the top of the plot.

3. Macro Lens Modeling

Our microlensing analysis required a model of the strong (macro) lensing in the system. WFI2026 has been previously

Table 2
Convergence, Shear, and Stellar Convergence Fraction κ_*/κ for Each Lens Model

$f_{M/L}$	Convergence κ				Shear γ				κ_*/κ				χ^2/N_{dof}
	A1	A2	B	C	A1	A2	B	C	A1	A2	B	C	
0.1	0.90	0.91	0.88	0.91	0.08	0.11	0.06	0.14	0.04	0.05	0.02	0.05	3.60
0.2	0.85	0.86	0.83	0.86	0.12	0.16	0.09	0.20	0.04	0.05	0.02	0.05	2.85
0.3	0.76	0.78	0.72	0.78	0.20	0.27	0.14	0.34	0.11	0.13	0.07	0.13	3.10
0.4	0.70	0.71	0.65	0.70	0.26	0.34	0.18	0.42	0.15	0.16	0.10	0.16	3.16
0.5	0.63	0.65	0.57	0.64	0.31	0.42	0.21	0.52	0.20	0.22	0.13	0.21	2.82
0.6	0.56	0.58	0.50	0.57	0.37	0.49	0.25	0.61	0.26	0.28	0.18	0.27	2.89
0.7	0.51	0.53	0.44	0.52	0.41	0.56	0.28	0.69	0.31	0.34	0.21	0.33	2.77
0.8	0.40	0.43	0.31	0.42	0.50	0.68	0.35	0.84	0.56	0.59	0.43	0.58	2.89
0.9	0.33	0.36	0.23	0.35	0.56	0.76	0.38	0.94	0.75	0.77	0.64	0.77	2.87
1.0	0.26	0.30	0.16	0.29	0.61	0.83	0.42	1.03	1.00	1.00	1.00	1.00	2.84

Note. The parameter $f_{M/L}$ indicates the strength of the de Vaucouleurs moment relative to a de Vaucouleurs-only model, providing a proxy for the luminous matter fraction. The values for κ, γ, and κ_*/κ are calculated at the position of each image. The final column, χ^2/N_{dof}, indicates the relative fit of the model across all images.

modeled in Sluse et al. (2012) and Bate et al. (2018). In both cases, the authors found the need for significant external shear, but achieved good fits using a singular isothermal ellipsoid with shear (SIE+γ) model. From the isothermal ellipsoid models of Sluse et al. (2012) and Bate et al. (2018) we estimated the velocity dispersion in the lens.

Following the convention of previous multi-epoch studies (e.g., Morgan et al. 2018), we also modeled the lens with a sequence of two-component de Vaucouleurs and Navarro, Frenk, and White (NFW; Navarro et al. 1997) models with external shear. This simulated the expected profiles of stellar matter (de Vaucouleurs) and dark matter (NFW) and allowed us to marginalize over the unknown dark matter fraction. We used the `LENSMODEL` software (Keeton 2001), omitting constraints from the flux ratios, which can be influenced by microlensing. Our first model employed a pure de Vaucouleurs profile (100% stellar matter) to fit for the centroid, moment, ellipticity, position angle, effective radius, and shear strength and orientation of the lens galaxy. We call this model $f_{M/L} = 1.0$, where we define $f_{M/L}$ as the fractional strength of the de Vaucouleurs moment relative to a unity mass-to-light-ratio model. We then reduced the de Vaucouleurs moment in increments of 10% and added an NFW component fixed to the same lens centroid, ellipticity, and position angle, and refit for all parameters. This generated a 10 model sequence with $f_{M/L} = 0.10$–1.0 in increments of 0.1, nominally spanning the range of 0%–90% dark matter, and permitted our analysis to marginalize over the unknown dark matter fraction. An advantage of using a wide range of dark matter fractions is that it also effectively samples a wide range of possible lens galaxy profile shapes. This is especially important for WFI2026 given the broad errors in Table 1, which can predict very different stellar-mass fractions. Best fits for the convergence, κ, and shear, γ, and stellar-to-total-convergence ratio, κ_*/κ, of this sequence are given in Table 2. We also show the relative quality of fit, which varies little between models.

A shortcoming of our WFI2026 lens model sequence is the unknown lens redshift, z_l. In the discovery paper, Morgan et al. (2004) favor a lens redshift of $z_l = 0.4$, based upon lens galaxy luminosity. However, in a more recent study Mosquera & Kochanek (2011) used astrometry-based methods (Ofek et al. 2003) to estimate a lens redshift of $z_l = 1.04$. As our VLT spectra showed no apparent lens galaxy features, we were unable to independently measure the redshift. We note that the lack of any lens galaxy signal in the spectrum is consistent with a featureless UV continuum of a $z_l = 1.04$ or greater elliptical galaxy. In our analysis we adopted the more recent estimate of $z_l = 1.04$ as the nominal lens redshift, but we also examined the impact of instead using $z_l = 0.4$ in Section 5.1.

Table 3
Time Delays Used for the Microlensing Analysis

Source	τ_{B-A} (days)	τ_{B-C} (days)
Euler ECAM	$18.7^{+4.1}_{-4.3}$	⋯
Lens Models	⋯	$23.7^{+5.2}_{-5.2}$

We attempted to measure the time delays using the `PyCS` algorithm of Tewes et al. (2013), which performed very well in a recent time-delay challenge (Liao et al. 2015; Bonvin et al. 2016). `PyCS` has been adopted as the curve-shifting algorithm of choice for COSMOGRAIL. Details of the WFI2026 measurement will be included as part of a larger set of time delay measurements in a forthcoming paper (M. Millon et al. 2019, in preparation). Here we report only the resulting time delays, shown in Table 3. The time delays are consistent with models at $z = 1.04$ but not at $z = 0.4$, lending further support to the larger lens redshift. The empirical time delays for image C were highly uncertain, and inconsistent between A–C and B–C. As such, we retained only the A–B measurement in our microlensing analysis. For image C, we instead used the $z = 1.04$ lens model that best matched the empirical A–B delay, and extrapolated the model results to estimate a time delay. We explored the impact of time delay uncertainty on our disk size measurement in Section 5.1.

4. Microlensing Models

Our microlensing analysis was based on the procedure developed in Kochanek (2004) and Kochanek et al. (2006). This technique uses Monte Carlo methods to fit the observed microlensing lightcurves from trajectories through a set of stellar magnification fields.

Before running our analysis, we binned the lightcurves in a 20 day window, using error-weighted mean magnitude and mean Heliocentric Julian Date (HJD). This decreased the number of epochs from 548 to 129, which kept calculation times reasonable for the subsequent Monte Carlo analysis. Because Mosquera & Kochanek (2011) estimated a source-

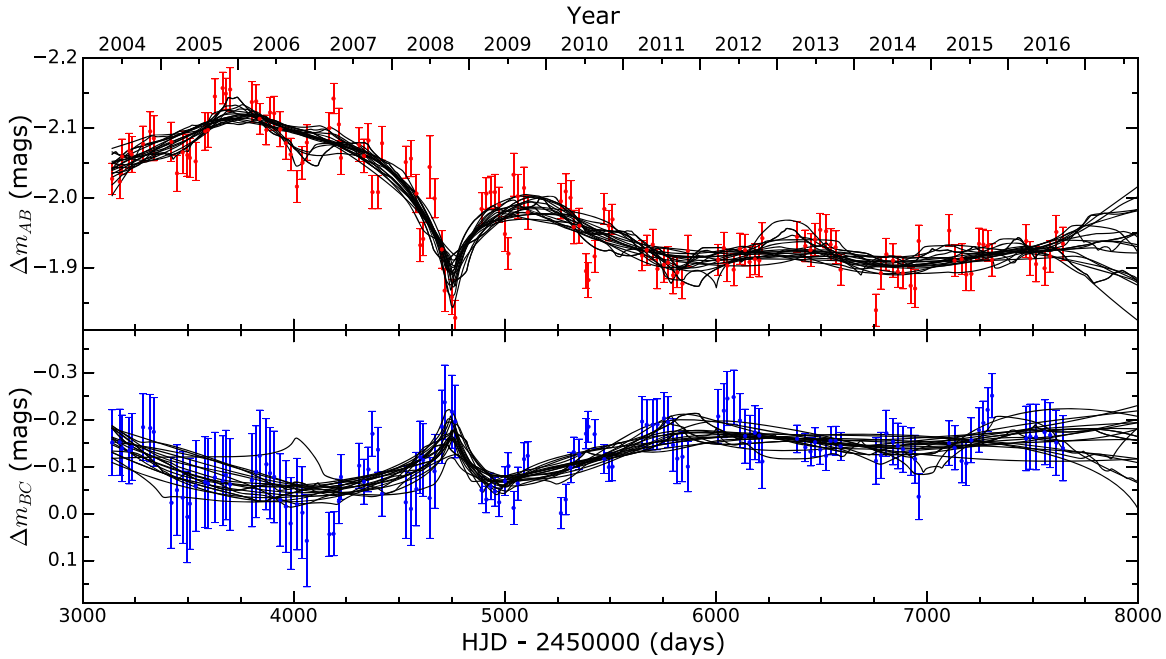

Figure 4. The 20 best-fit curves from our microlensing analysis. Top: time-delay-corrected difference curves for images A–B, $\Delta m_{AB} = m_A - m_B$, in magnitudes. Bottom: the difference curves for images B–C, $\Delta m_{BC} = m_B - \langle m_C \rangle$, where $\langle m_C \rangle$ is the season average for image C. All curves fit the strong microlensing feature from image B near HJD-2,450,000 = 4700 days. They also consistently fit the slow gradient between HJD-2,450,000 ∼3500–6000 days.

crossing timescale of 1.4 yr in WFI2026 and a longer Einstein-radius-crossing timescale of 26.6 yr, we were not concerned about microlensing on a sub-monthly scale. These short timescales are also not well-resolved for typical trajectories across the microlensing patterns. To further mitigate the impact of short-timescale noise on the microlensing solution, we included systematic errors of 0.015 mag to account for any unmodeled photometric errors.

We shifted each curve by the time delays, holding the lightcurve for B as a fixed reference and linearly interpolating for images A and C. We averaged over the time-delay-shifted season C values as detailed in Section 2. The magnitude differences are shown in Figure 4 for B–A (top panel, red) and B–C (bottom panel, blue). Microlensing is the dominant source of time variability between these time-delay-shifted difference lightcurves.

In a dynamic microlensing analysis, the magnification curve, $\mu(t)$, depends on highly nonlinear magnification by a stellar field in the lens galaxy. Because we cannot measure the precise stellar characteristics in the lens galaxy, we generated many possible magnification patterns at the range of κ_*/κ from our model sequence (see Table 2). As with previous studies, we assumed a stellar-mass distribution of $dN/dM \propto M^{-1.3}$, a ratio of maximum over minimum mass of 50, and a variable median microlensing mass $\langle M_*/M_\odot \rangle$. We projected the stellar magnification patterns on a 8192 × 8192 grid that spanned sizes from $40R_{\rm E}$ down to the pixel scale, $\sim 0.005\,R_{\rm E}$. Here $R_{\rm E} = D_{OS}\theta_{\rm E}$, where D_{OS} is the angular diameter distance from the observer to the source and $\theta_{\rm E} \propto \langle M_*/M_\odot \rangle^{1/2}$ is the Einstein radius as a function of median stellar microlens mass.

For each of the 10 macro models ($0.1 \leqslant f_{\rm M/L} \leqslant 1.0$), we generated 40 magnification patterns for each lensed image, yielding 400 complete sets of magnification patterns. This eliminated concerns about the introduction of systematics from repetitive use of one or a small number of patterns for a given image location and macro model. We created fits to the combined image A = A1+A2 lightcurve by summing the model lightcurves generated separately from the magnification patterns for images A1 and A2. The goodness-of-fit to each point in the summed lightcurve A was assigned the same statistical weight as each point in the resolved lightcurves for images B and C.

To model the disk radius, we convolved each magnification pattern with a Gaussian kernel at a range of trial accretion disk sizes. We chose 17 radii evenly spaced in the logarithmic range $\log(r/{\rm cm}) = 14.5$–18.5. Since Mortonson et al. (2005) showed that the half-light radius, rather than profile shape, affects the inferred microlensing size, we selected the Gaussian profile rather than the thin-disk model for speed of calculation. Upon conclusion of the analysis, we converted the best-fit Gaussian scale radius to a thin-disk scale radius r_s.

We generated trial lightcurves by moving a point source across a convolved magnification pattern. We selected transverse velocities from the logarithmic range $10\ {\rm km\ s^{-1}} \leqslant \hat{v}_e \langle M_*/M_\odot \rangle^{1/2} \leqslant 10^6\ {\rm km\ s^{-1}}$ and randomized the directions and starting points in each image. From these trajectories, we found the magnification as a function of time and compared this to our empirical lightcurves using a χ^2 statistic. We allowed for a 0.5 mag systematic uncertainty in the intrinsic flux ratios between the images to account for the influence of substructure and broad-line region contamination. We terminated a trial when $\chi^2/N_{\rm dof} > 1.4$, where $N_{\rm dof}$ is the number of degrees of freedom, as these solutions did not contribute significant statistical weight to the inferred parameter values. In the Monte Carlo phase of our analysis, we used the United States Naval Academy High Performance Cluster[7] to attempt 10^7 trials on each of the 400 magnification patterns for a grand total of 4×10^9 trials. Additional trials did not significantly improve constraints.

[7] https://www.usna.edu/ARCS/

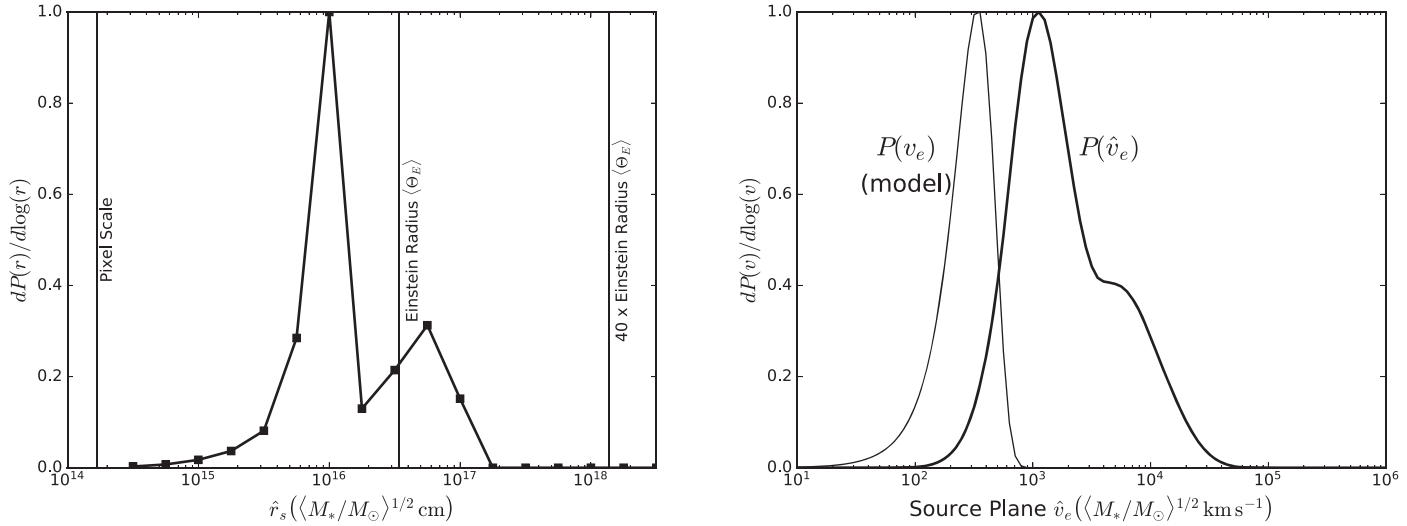

Figure 5. Effective source radius and velocity inferred from the WFI2026 microlensing analysis. Left: probability density for the scale radius, $\hat{r}_s$ in Einstein units, scaled to a 1 $M_\odot$ median microlensing mass. Right: the probability density function for the effective quasar velocity, $\hat{v}_e$ in Einstein units, scaled to a 1 $M_\odot$ median microlensing mass. The thicker curve indicates the value found from the microlensing analysis and shows the same bimodality seen in the probability density for the radius. The thin curve indicates our cosmological velocity model, v_e, in km s^{-1}.

5. Results

In this section we present our microlensing analysis and show our determination of the size of WFI2026, reported as the scale radius r_s. We also present our analysis of the VLT spectra to determine the mass of the black hole.

5.1. Microlensing

Several of the best fits to the time-delay-corrected curves are shown in Figure 4. We can see strong microlensing variability in this system on the order of ∼0.2 mag over the 13 seasons. There is also a short duration, high-magnification event in image B rising across the entire 2008 season. The best-fit curves consistently reproduced these dominant microlensing features.

We calculated probability densities for the variables of interest by marginalizing over the other variables of the model. For the radius, this took the form

$$P(\hat{r}_s|D) \propto \int_0^\infty P(D|\hat{r}_s, \xi)\pi(\xi)\pi(\hat{r}_s)d\xi. \quad (2)$$

where ξ represents all other variables, including effective source velocity, $\hat{v}_e$ and luminous matter fraction, $f_{\mathrm{M/L}}$. The prior distribution is captured in $\pi(\xi)$ and is, for example, log-uniform for $\hat{v}_e$ on [10, 10^6] and uniform for $f_{\mathrm{M/L}}$ on [0.1, 1], while the prior $\pi(\hat{r}_s)$ is log-uniform on [$10^{14.5}$, $10^{18.5}$]. The probability of the data $P(D|\hat{r}_s, \xi)$ is equivalent to $P(\chi^2|N_{\mathrm{dof}})$ in Equation (10) of Kochanek (2004).

In Figure 5, we display the resulting probability density for the primary variable of interest, the source size $\hat{r}_s = r_s\langle M_*/M_\odot\rangle^{-1/2}$. The $\hat{r}_s$ distribution is in Einstein units, scaled assuming a 1 $M_\odot$ median stellar mass in the lens galaxy. To convert this result to physical units, we convolve $\hat{r}_s$ with the probability density for $\langle M_*/M_\odot\rangle$, where the $\langle M_*/M_\odot\rangle$ distribution is found as in Kochanek (2004) by

$$P(\langle M_*/M_\odot\rangle|D) \propto \int P(\hat{v}_e|D)P(v_e)dv_e \quad (3)$$

where $\hat{v}_e = v_e\langle M_*/M_\odot\rangle^{-1/2}$. The velocity probability density distributions are shown in the right panel of Figure 5. Because $\hat{v}_e$ is more finely sampled than $\hat{r}_s$, the resulting distribution is much smoother.

To find $P(v_e)$, the probability density for the actual source velocity, we model the effective source velocity v_e following the method of Kochanek (2004) and using the formulation of Mosquera & Kochanek (2011). This includes velocity contributions from the observer, v_{CMB}, source, $\sigma_{\mathrm{pec}}(z_s)$, lens bulk motion, $\sigma_{\mathrm{pec}}(z_l)$, and lens velocity dispersion, σ_*. We projected the CMB dipole along the line of sight to WFI2026 to find the north and east vector components of v_{CMB} as -227 km s^{-1} and -244 km s^{-1}, respectively. For the bulk galaxy motions we used cosmological models to estimate the one-dimensional peculiar velocity dispersions to be $\sigma_{\mathrm{pec}}(z_l) = 265$ km s^{-1} and $\sigma_{\mathrm{pec}}(z_s) = 204$ km s^{-1}. We also included a contribution of $\sigma_* = 335$ km s^{-1} from the stellar velocity dispersion in the lens, determined from the Einstein radius found by Sluse et al. (2012) with an SIE+γ lens model.

With our inferred distribution for $\langle M_*/M_\odot\rangle$ we estimated the probability density function for the accretion disk size in physical units, r_s, shown with the solid line in Figure 6. Adopting a nominal inclination of $\langle\cos(i)\rangle = 0.5$ for ready comparison to other microlensing studies (e.g., Blackburne et al. 2011; Morgan et al. 2018), the scale radius of the WFI2026 accretion disk at $\lambda_{\mathrm{rest}} = 2043$ Å is $\log\{(r_s/\mathrm{cm})[\cos(i)/0.5]^{-1/2}\} = 15.74^{+0.34}_{-0.29}$. This result can be easily rescaled to any inclination, such as a smaller angle of $\lesssim$30° that may be more typical of quasars under unification models (e.g., Urry & Padovani 1995; Wills & Brotherton 1995).

To examine the impact of uncertainty in the median microlensing mass distribution, we also experimented with applying a uniform mass prior of $0.1 < \langle M_*/M_\odot\rangle < 1.0$, resulting in the distribution with the dotted line in Figure 6. The mass prior narrows the distribution marginally, but nonetheless provides a fully consistent result. For self-consistency, we adopt the distribution without the mass prior as our primary result.

We found a bimodal distribution in both $dP(\hat{r}_s)/d\log(\hat{r}_s)$ and $dP(\hat{v}_e)/d\log(\hat{v}_e)$ but see no evidence for bimodality in $dP(r_s)/d\log(r_s)$. We can understand this by examining the

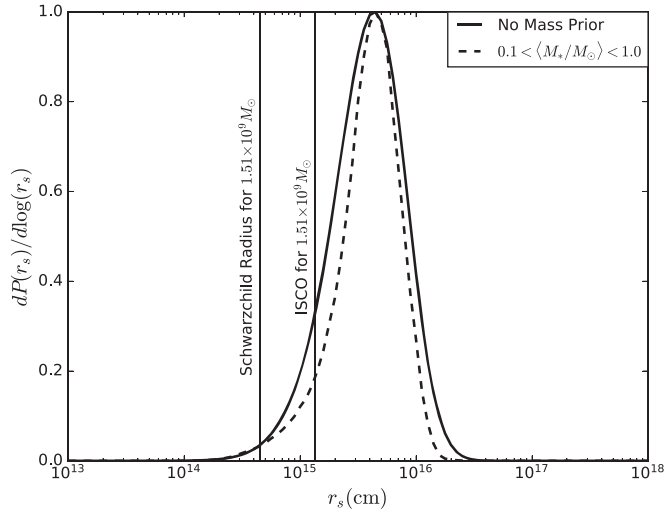

Figure 6. Accretion disk radius of WFI2026 $\lambda_{\rm rest} = 2043$ Å, displayed as a probability density for the scale radius in physical units. The solid line corresponds to the result with no prior on median microlensing mass. The dashed line is the solution with a uniform prior on the median microlensing mass of $0.1 < \langle M_*/M_\odot \rangle < 1.0$.

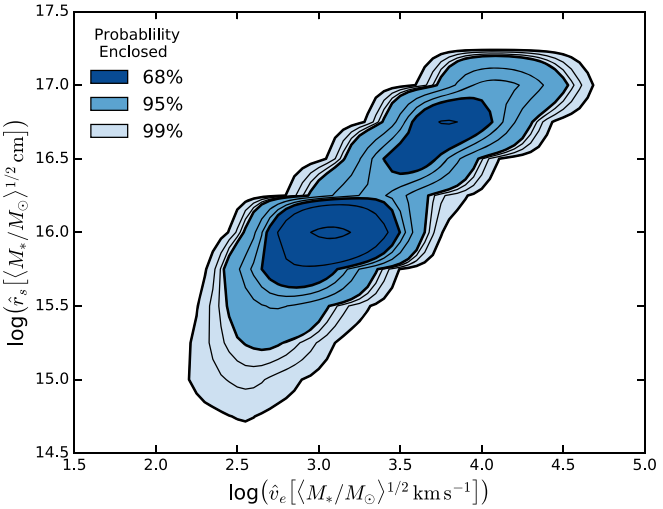

Figure 7. Probability contours of $\log(\hat{v}_e)$ vs. $\log(\hat{r}_s)$ for WFI2026. Confidence intervals enclosing 68%, 95%, and 99% of the total probability are shaded in blue. The bimodal peaks are evident here, as is an overall linear relation between $\log(\hat{v}_e)$ and $\log(\hat{r}_s)$.

underlying nature of the bimodal solutions. The high-velocity, large-radius mode corresponds to a low median microlensing mass. However, because the median microlensing mass is smaller for these solutions, the true value of $r_s = \hat{r}_s \langle M_*/M_\odot \rangle^{1/2}$, the product of mass and radius, remains relatively unchanged. Both modes return the same physical estimate in the limit of $\hat{v}_e \propto \hat{r}_s$. This relation is nearly satisfied by our solutions, as seen in the probability contours in Figure 7. This trend indicates that the data most strongly constrain the ratio of $\hat{v}_e/\hat{r}_s$, which is independent of $\langle M_*/M_\odot \rangle$. This insensitivity to the unknown microlensing mass is one of the strengths of multi-epoch lightcurve analysis.

As an additional verification, we reran the microlensing analysis with a log-uniform prior on the source velocity of $1.0 < \log \hat{v}_e < 4.0$. This disallowed unreasonably high-velocity solutions, providing a different means of imposing a lower limit on microlensing mass. In this second analysis, the velocity distribution had only a single mode, as expected, and the resulting size estimate was effectively unchanged.

We also tested the sensitivity of our results to the unknown lens redshift, z_l, by calculating the distances, velocities, and radii for the low and high estimates of the lens redshift, $0.4 < z_l < 1.04$. Given the lack of a caustic crossing in the WFI2026 lightcurves, the dominant timescale for microlensing variability is the Einstein-radius crossing time $t_E = R_E/v_e$. Because the physical radius $R_E \propto (D_{\rm LS} D_{\rm OS}/D_{\rm OL})^{1/2}$, the influence of the resulting sizes only scales as the square root of the change in the angular diameter distances. Comparing the physical size measurement between the two redshifts we found a change in $\log(r)$ of less than 2%, fully consistent within the statistical errors.

Similarly, our results are only weakly sensitive to the time delay. We repeated the microlensing analysis with low and high time delays based on the error limits in Table 3, but the resulting changes in our measurement of the scale radius were negligible.

We attempted to estimate the relative stellar-mass fraction by marginalizing over velocities and radii. There was a mild preference for the lowest stellar-mass models, but not significant enough to warrant a quantitative estimate.

5.2. Black Hole Mass

Our reduced VLT spectra for images A and B are shown in Figure 3 with several prominent emission lines indicated. Because of the relatively high source redshift, $z_s = 2.23$, the Mg II line is redshifted out of the observed frame. The C IV line is, however, fully resolved in both images and can be used to estimate black hole mass (Vestergaard & Peterson 2006; Park et al. 2013).

We first estimated the C IV emission line width in the spectra of image A and image B independently. Line widths were measured by fitting a local, linear continuum under the emission line and then determining the FWHM and the line dispersion or second moment, σ_l, directly from the data above the continuum (see Peterson et al. 2004 for a more detailed description). There is good agreement in the line widths determined from the spectra of the two separate images, with average values of FWHM $= 6015 \pm 40\,\mathrm{km\,s^{-1}}$ and $\sigma_l = 3616 \pm 4\,\mathrm{km\,s^{-1}}$.

Vestergaard & Peterson (2006) and Park et al. (2013) provide prescriptions for estimating black hole masses based on the C IV emission line that are calibrated to the Hβ reverberation mapping results for local AGNs. Work by Denney et al. (2013) shows that single-epoch black hole masses derived from the C IV emission line are less biased when adopting σ_l as the line width measurement rather than FWHM, so we focus on those prescriptions. The other necessary ingredient is the continuum luminosity at rest-frame 1350 Å, which was not covered in the VLT spectra of WFI 2026-4536. Fortunately, Vestergaard & Peterson (2006) show that $L_\lambda(1450\,\text{Å})$ can be directly substituted for $L_\lambda(1350\,\text{Å})$.

We measured continuum flux densities of $f_\lambda(1450 \times (1+z)) = 1.3 \times 10^{-15}$ erg s^{-1} cm^{-2} Å^{-1} for image B and 6.9×10^{-15} erg s^{-1} cm^{-2} Å^{-1} for image A. Allowing for the range of image magnifications spanned by the model sequence in Table 2, and accounting for Galactic extinction along the line of sight, we find $\log(\lambda L_\lambda(1450\,\text{Å})/\mathrm{erg\,s^{-1}}) = 46.523^{+0.388}_{-0.155}$. Combined with the emission line width and using the

prescriptions of Vestergaard & Peterson (2006) we estimate $\log(M_{\rm BH}/M_\odot) = 9.18^{+0.39}_{-0.34}$, including in our uncertainty the 0.33 dex of scatter reported for their prescription. The black hole mass estimate is nearly identical if the prescriptions of Park et al. (2013) are adopted instead.

6. Discussion and Conclusions

The key measurement we have presented in this study is the accretion disk size of WFI2026, shown in Figure 6. Our findings with and without a prior on microlensing mass are consistent, so this result is essentially independent of the unknown median microlensing mass. To compare our measurement to those from other studies on WFI2026, we convert this to a half-light radius, under the thin-disk assumption, to give a value of $\log\{(r_{1/2}/{\rm cm})[\cos(i)/0.5]^{-1/2}\} = 16.13^{+0.34}_{-0.29}$. Our estimate is smaller, but consistent with the findings of Blackburne et al. (2011), $\log(r_{1/2}/{\rm cm}) = 16.46 \pm 0.32$, and larger than the estimate $\log(r_{1/2}/{\rm cm}) < 16$ found by Bate et al. (2018), but again, consistent within statistical bounds. The estimate from Bate et al. (2018) adjusts the half-light radius based on their empirical temperature slope rather than thin-disk slope. If instead, we adjust their scale size based on thin-disk scaling, their estimate increases to $\log(r_{1/2}/{\rm cm}) < 16.14$, fully consistent with our measurement.

Although we found a well-constrained measurement of the physical accretion disk size, we did encounter a bimodal distribution in the effective radius and source velocity, which was mitigated by the degeneracy between $\hat{v}_e$ and $\hat{r}_s$. In any case, the application of a velocity prior validated these results.

We also reported the first spectroscopic measurement of the central black hole mass based on the C IV line width and the relation from Vestergaard & Peterson (2006). This is a relatively large central black hole, the second most massive in our sample of 15 quasars. Our estimate of $\log(M_{\rm BH}/M_\odot) = 9.18^{+0.39}_{-0.34}$ is larger than the bolometric luminosity estimate from Blackburne et al. (2011) of $\log(M_{\rm BH}/M_\odot) = 8.90$ in accordance with their findings that luminosity-based estimates are systematically smaller than virial estimates that also use the broad emission line width.

With our black hole mass estimate, we compared our results from WFI2026 to the r_μ versus $M_{\rm BH}$ relation from Morgan et al. (2010, 2018). To match this study, we shifted our scale radius to $\lambda_{\rm rest} = 2500$ Å, assuming a thin-disk model, which gave $\log(r_s/{\rm cm}[\cos(i)/0.5]^{-1/2}) = 15.86^{+0.34}_{-0.29}$. This value is fully consistent with the estimate of $\log(r_{2500}/{\rm cm}) = 15.97 \pm 0.12$ predicted by the accretion disk size—$M_{\rm BH}$ relation of Morgan et al. (2018), as can be seen in Figure 8.

Figure 8 also shows that the microlensing sizes are systematically larger than the theoretical thin-disk sizes one would predict using standard thin-disk theory (see Morgan et al. (2010) for details). Following the same approach and using the Magellan *i*-band flux from Morgan et al. (2004), we estimated the luminosity size for WFI2026. Adopting an inclination angle of 60°, we found $\log\{(r_L/{\rm cm})[\cos(i)/0.5]^{-1/2}\} = 15.08 \pm 0.13$, when rescaled to a rest-frame wavelength of 2500 Å. This estimate is smaller than the microlensing size measurements by 0.66 ± 0.33 dex, similar to the offset reported in previous microlensing studies.

The general consistency of these 15 studies offers an opportunity to infer host quasar properties. In a forthcoming work, we will use the observed size offset and the framework developed in Morgan et al. (2010) to provide a robust observational constraint on the quasar accretion disk temperature profile.

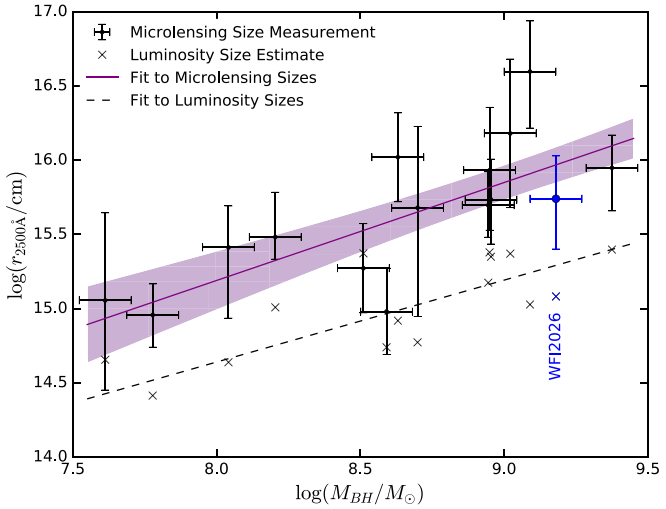

Figure 8. Quasar accretion disk sizes scaled to $\lambda_{\rm rest} = 2500$ Å plotted as a function of the central black hole masses. WFI2026 is highlighted in blue, while the other available microlensing size measurements are shown as black dots (Kochanek 2004; Morgan et al. 2008, 2010, 2018, 2012; Dai et al. 2010; Hainline et al. 2012, 2013; MacLeod et al. 2015). The best-fit line from Morgan et al. (2018) is shown in purple with 1σ error bars encompassed by the purple band. The luminosity-based size estimates are shown with black diagonal crosses, with the best fit indicated by the black dotted line.

This material is based upon work supported by the National Science Foundation under grant AST-1614018 to M.A.C. and C.W.M.

COSMOGRAIL is made possible thanks to the continuous work of all observers and technical staff obtaining the monitoring observations, in particular, at the Swiss Leonhard Euler telescope at La Silla Observatory, which is supported by the Swiss National Science Foundation. M.M., F.C., and V.B. acknowledge support from the Swiss National Science Foundation (SNSF) and through European Research Council (ERC) under the European Unions Horizon 2020 research and innovation programme (COSMICLENS: grant agreement No. 787886).

M.C.B. gratefully acknowledges support from the National Science Foundation through CAREER grant AST-1253702 to Georgia State University.

We thank the anonymous referees for feedback that significantly improved this manuscript. We are grateful to Christopher S. Kochanek for the use of his microlensing analysis code.

Facilities: HST (NICMOS), VLT:Kueyen, Euler:1.2m.

Software: Anaconda, `LENSMODEL` (Keeton 2001), `PyCS` (Tewes et al. 2013).

Appendix
WFI2026 Lightcurve Table

We include here the full WFI2026 lightcurve used in this study (see Table A1).

Table A1
Reduced Lightcurve for WFI2026

HJD (days)	A = A1+A2 (mag)	B (mag)	C (mag)
3125.903	2.641 ± 0.006	4.686 ± 0.014	4.730 ± 0.029
3126.893	2.654 ± 0.002	4.694 ± 0.002	4.664 ± 0.048
3149.879	2.674 ± 0.010	4.612 ± 0.037	4.739 ± 0.058
3151.820	2.642 ± 0.004	4.667 ± 0.003	4.772 ± 0.030
3153.856	2.657 ± 0.008	4.604 ± 0.006	4.740 ± 0.038
3156.804	2.655 ± 0.008	4.673 ± 0.034	4.723 ± 0.059
3158.791	2.652 ± 0.005	4.677 ± 0.010	4.817 ± 0.054
3160.851	2.645 ± 0.001	4.646 ± 0.003	4.866 ± 0.031
3162.794	2.651 ± 0.001	4.654 ± 0.008	4.722 ± 0.075
3183.835	2.657 ± 0.004	4.673 ± 0.011	4.786 ± 0.019
3194.875	2.646 ± 0.004	4.702 ± 0.009	4.865 ± 0.026
3197.851	2.627 ± 0.010	4.701 ± 0.037	4.889 ± 0.058
3203.861	2.627 ± 0.003	4.705 ± 0.011	4.871 ± 0.012
3226.768	2.630 ± 0.010	4.672 ± 0.037	4.765 ± 0.058
3241.782	2.645 ± 0.005	4.685 ± 0.009	4.732 ± 0.071
3245.776	2.614 ± 0.003	4.662 ± 0.016	4.952 ± 0.015
3248.711	2.621 ± 0.003	4.655 ± 0.021	4.819 ± 0.015
3294.634	2.564 ± 0.010	4.654 ± 0.037	4.852 ± 0.058
3296.612	2.555 ± 0.005	4.674 ± 0.011	4.878 ± 0.018
3302.557	2.563 ± 0.001	4.634 ± 0.008	4.807 ± 0.009
3303.590	2.566 ± 0.003	4.608 ± 0.021	4.804 ± 0.017
3309.548	2.557 ± 0.010	4.609 ± 0.037	4.810 ± 0.058
3310.599	2.570 ± 0.005	4.629 ± 0.005	4.752 ± 0.042
3329.540	2.538 ± 0.010	4.619 ± 0.037	4.740 ± 0.058
3334.564	2.556 ± 0.010	4.698 ± 0.037	4.602 ± 0.058
3346.579	2.549 ± 0.010	4.631 ± 0.037	4.641 ± 0.058
3353.559	2.566 ± 0.010	4.659 ± 0.037	4.519 ± 0.058
3431.853	2.490 ± 0.018	4.580 ± 0.005	4.514 ± 0.017
3432.861	2.513 ± 0.011	4.561 ± 0.040	4.379 ± 0.028
3433.889	2.496 ± 0.005	4.564 ± 0.023	4.502 ± 0.015
3434.865	2.491 ± 0.005	4.575 ± 0.006	4.477 ± 0.044
3435.868	2.507 ± 0.010	4.580 ± 0.037	4.384 ± 0.058
3436.865	2.528 ± 0.003	4.550 ± 0.018	4.421 ± 0.008
3442.836	2.501 ± 0.010	4.569 ± 0.037	4.527 ± 0.058
3450.857	2.533 ± 0.009	4.599 ± 0.009	4.563 ± 0.062
3458.874	2.533 ± 0.000	4.527 ± 0.018	4.579 ± 0.007
3467.914	2.506 ± 0.010	4.623 ± 0.037	4.595 ± 0.058
3480.856	2.510 ± 0.005	4.660 ± 0.017	4.676 ± 0.031
3499.763	2.558 ± 0.010	4.528 ± 0.037	4.761 ± 0.058
3502.793	2.569 ± 0.005	4.551 ± 0.035	4.694 ± 0.019
3511.813	2.557 ± 0.006	4.602 ± 0.020	4.727 ± 0.047
3516.799	2.578 ± 0.010	4.527 ± 0.037	4.716 ± 0.058
3520.882	2.538 ± 0.010	4.617 ± 0.037	4.852 ± 0.058
3522.892	2.541 ± 0.000	4.573 ± 0.013	4.813 ± 0.005
3524.907	2.531 ± 0.001	4.558 ± 0.015	4.734 ± 0.019
3525.890	2.529 ± 0.003	4.586 ± 0.023	4.802 ± 0.009
3544.801	2.499 ± 0.010	4.483 ± 0.037	4.863 ± 0.058
3558.682	2.510 ± 0.007	4.555 ± 0.016	4.613 ± 0.035
3586.749	2.478 ± 0.005	4.600 ± 0.012	4.871 ± 0.008
3592.514	2.502 ± 0.011	4.551 ± 0.004	4.653 ± 0.033
3597.565	2.499 ± 0.010	4.507 ± 0.037	4.668 ± 0.058
3601.641	2.468 ± 0.010	4.404 ± 0.037	4.820 ± 0.058
3602.683	2.454 ± 0.001	4.522 ± 0.029	4.761 ± 0.009
3603.740	2.453 ± 0.003	4.564 ± 0.011	4.749 ± 0.015
3607.568	2.470 ± 0.007	4.540 ± 0.015	4.667 ± 0.021
3608.627	2.456 ± 0.002	4.519 ± 0.000	4.690 ± 0.031
3614.801	2.451 ± 0.010	4.535 ± 0.044	4.529 ± 0.007
3634.705	2.407 ± 0.010	4.530 ± 0.037	4.534 ± 0.058
3640.716	2.396 ± 0.005	4.563 ± 0.000	4.518 ± 0.020
3645.611	2.399 ± 0.004	4.424 ± 0.015	4.525 ± 0.027
3650.583	2.393 ± 0.003	4.540 ± 0.006	4.645 ± 0.008
3668.524	2.408 ± 0.001	4.454 ± 0.005	4.570 ± 0.043
3672.554	2.391 ± 0.003	4.543 ± 0.013	4.609 ± 0.009
3675.528	2.405 ± 0.002	4.548 ± 0.023	4.443 ± 0.009

Table A1
(Continued)

HJD (days)	A = A1+A2 (mag)	B (mag)	C (mag)
3676.543	2.386 ± 0.010	4.535 ± 0.037	4.583 ± 0.058
3677.572	2.383 ± 0.003	4.549 ± 0.007	4.589 ± 0.008
3678.537	2.385 ± 0.001	4.550 ± 0.010	4.629 ± 0.005
3680.542	2.398 ± 0.003	4.522 ± 0.009	4.500 ± 0.006
3681.572	2.403 ± 0.010	4.521 ± 0.037	4.459 ± 0.058
3682.585	2.374 ± 0.005	4.547 ± 0.002	4.544 ± 0.011
3684.547	2.368 ± 0.003	4.562 ± 0.019	4.564 ± 0.007
3685.572	2.377 ± 0.010	4.520 ± 0.037	4.551 ± 0.058
3686.545	2.394 ± 0.000	4.527 ± 0.009	4.505 ± 0.021
3687.545	2.371 ± 0.001	4.561 ± 0.011	4.579 ± 0.006
3688.578	2.381 ± 0.010	4.559 ± 0.006	4.589 ± 0.007
3689.530	2.387 ± 0.001	4.554 ± 0.013	4.468 ± 0.015
3690.532	2.388 ± 0.005	4.509 ± 0.029	4.476 ± 0.009
3691.572	2.382 ± 0.002	4.571 ± 0.008	4.484 ± 0.012
3692.558	2.382 ± 0.002	4.557 ± 0.009	4.528 ± 0.007
3693.532	2.379 ± 0.010	4.534 ± 0.037	4.594 ± 0.058
3694.525	2.375 ± 0.004	4.552 ± 0.003	4.584 ± 0.011
3695.530	2.388 ± 0.010	4.533 ± 0.037	4.509 ± 0.058
3696.542	2.398 ± 0.002	4.472 ± 0.006	4.564 ± 0.029
3700.535	2.382 ± 0.006	4.547 ± 0.016	4.537 ± 0.025
3707.540	2.404 ± 0.003	4.493 ± 0.010	4.489 ± 0.013
3715.527	2.401 ± 0.009	4.600 ± 0.044	4.501 ± 0.032
3806.865	2.426 ± 0.010	4.536 ± 0.037	4.511 ± 0.058
3813.826	2.436 ± 0.005	4.601 ± 0.037	4.342 ± 0.008
3819.852	2.419 ± 0.003	4.551 ± 0.020	4.523 ± 0.016
3820.811	2.420 ± 0.010	4.615 ± 0.037	4.416 ± 0.058
3821.848	2.408 ± 0.003	4.553 ± 0.010	4.641 ± 0.018
3824.855	2.423 ± 0.003	4.529 ± 0.011	4.491 ± 0.011
3828.903	2.379 ± 0.001	4.543 ± 0.003	4.589 ± 0.008
3829.844	2.387 ± 0.010	4.560 ± 0.037	4.522 ± 0.058
3831.859	2.411 ± 0.009	4.507 ± 0.005	4.445 ± 0.012
3832.870	2.421 ± 0.002	4.493 ± 0.002	4.450 ± 0.008
3835.907	2.405 ± 0.002	4.513 ± 0.008	4.546 ± 0.025
3845.898	2.433 ± 0.004	4.407 ± 0.016	4.560 ± 0.023
3846.892	2.423 ± 0.003	4.479 ± 0.004	4.508 ± 0.029
3847.867	2.407 ± 0.002	4.510 ± 0.011	4.579 ± 0.005
3848.853	2.404 ± 0.002	4.541 ± 0.022	4.494 ± 0.014
3849.858	2.400 ± 0.003	4.554 ± 0.013	4.572 ± 0.011
3850.899	2.389 ± 0.001	4.521 ± 0.005	4.629 ± 0.005
3851.868	2.388 ± 0.001	4.559 ± 0.003	4.640 ± 0.009
3852.881	2.415 ± 0.004	4.487 ± 0.011	4.559 ± 0.004
3869.840	2.419 ± 0.004	4.450 ± 0.002	4.576 ± 0.009
3873.818	2.429 ± 0.001	4.504 ± 0.007	4.538 ± 0.024
3886.896	2.433 ± 0.003	4.546 ± 0.001	4.685 ± 0.025
3887.896	2.426 ± 0.002	4.514 ± 0.006	4.704 ± 0.005
3889.851	2.431 ± 0.005	4.456 ± 0.012	4.670 ± 0.029
3891.891	2.415 ± 0.002	4.539 ± 0.003	4.692 ± 0.009
3892.878	2.414 ± 0.005	4.525 ± 0.006	4.715 ± 0.008
3893.936	2.416 ± 0.001	4.559 ± 0.002	4.606 ± 0.034
3900.817	2.398 ± 0.007	4.499 ± 0.038	4.613 ± 0.019
3908.773	2.418 ± 0.001	4.438 ± 0.004	4.666 ± 0.008
3913.766	2.429 ± 0.002	4.451 ± 0.005	4.673 ± 0.012
3917.614	2.443 ± 0.010	4.542 ± 0.037	4.526 ± 0.058
3919.805	2.426 ± 0.010	4.489 ± 0.037	4.709 ± 0.058
3925.644	2.426 ± 0.002	4.579 ± 0.025	4.507 ± 0.010
3932.862	2.445 ± 0.008	4.621 ± 0.008	4.630 ± 0.043
3944.684	2.503 ± 0.003	4.451 ± 0.006	4.670 ± 0.006
3945.832	2.478 ± 0.002	4.636 ± 0.013	4.781 ± 0.008
3946.781	2.505 ± 0.003	4.601 ± 0.010	4.708 ± 0.029
3950.688	2.500 ± 0.000	4.553 ± 0.004	4.805 ± 0.016
3952.765	2.532 ± 0.010	4.649 ± 0.037	4.742 ± 0.058
3957.597	2.519 ± 0.010	4.572 ± 0.037	4.712 ± 0.058
3961.790	2.511 ± 0.003	4.686 ± 0.015	4.812 ± 0.017
3964.569	2.545 ± 0.001	4.604 ± 0.002	4.528 ± 0.013

Table A1
(Continued)

HJD (days)	A = A1+A2 (mag)	B (mag)	C (mag)
3970.695	2.578 ± 0.004	4.469 ± 0.024	4.520 ± 0.032
3979.618	2.533 ± 0.004	4.654 ± 0.012	4.828 ± 0.025
3980.746	2.551 ± 0.007	4.662 ± 0.010	4.664 ± 0.031
3981.724	2.531 ± 0.001	4.665 ± 0.003	4.899 ± 0.013
3982.726	2.526 ± 0.004	4.685 ± 0.035	4.844 ± 0.016
3994.581	2.547 ± 0.010	4.658 ± 0.037	4.829 ± 0.058
3998.601	2.563 ± 0.008	4.679 ± 0.020	4.693 ± 0.066
3999.582	2.573 ± 0.010	4.599 ± 0.037	4.773 ± 0.058
4003.582	2.555 ± 0.001	4.665 ± 0.010	4.855 ± 0.013
4005.568	2.592 ± 0.000	4.598 ± 0.003	4.704 ± 0.005
4008.645	2.532 ± 0.004	4.730 ± 0.009	4.920 ± 0.017
4024.629	2.588 ± 0.002	4.636 ± 0.012	4.637 ± 0.023
4025.577	2.591 ± 0.004	4.655 ± 0.002	4.581 ± 0.080
4026.575	2.579 ± 0.010	4.653 ± 0.037	4.679 ± 0.058
4027.559	2.586 ± 0.006	4.590 ± 0.022	4.650 ± 0.024
4028.558	2.582 ± 0.007	4.646 ± 0.009	4.589 ± 0.041
4032.539	2.573 ± 0.001	4.588 ± 0.001	4.667 ± 0.023
4036.530	2.564 ± 0.001	4.638 ± 0.008	4.825 ± 0.006
4039.535	2.559 ± 0.010	4.660 ± 0.037	4.742 ± 0.058
4042.519	2.600 ± 0.000	4.607 ± 0.003	4.546 ± 0.008
4046.511	2.571 ± 0.008	4.641 ± 0.023	4.753 ± 0.051
4057.520	2.578 ± 0.004	4.671 ± 0.002	4.653 ± 0.044
4061.531	2.573 ± 0.003	4.679 ± 0.014	4.750 ± 0.014
4065.523	2.585 ± 0.007	4.714 ± 0.037	4.607 ± 0.008
4072.535	2.605 ± 0.003	4.722 ± 0.013	4.628 ± 0.011
4076.536	2.610 ± 0.017	4.719 ± 0.014	4.622 ± 0.044
4086.531	2.611 ± 0.010	4.880 ± 0.037	4.626 ± 0.058
4174.872	2.652 ± 0.005	4.829 ± 0.008	4.652 ± 0.023
4183.867	2.646 ± 0.006	4.733 ± 0.002	4.682 ± 0.032
4191.873	2.653 ± 0.003	4.720 ± 0.005	4.707 ± 0.025
4192.859	2.647 ± 0.002	4.793 ± 0.004	4.729 ± 0.030
4197.832	2.642 ± 0.005	4.759 ± 0.031	4.543 ± 0.069
4200.872	2.612 ± 0.002	4.710 ± 0.009	4.688 ± 0.022
4203.855	2.605 ± 0.001	4.728 ± 0.002	4.681 ± 0.014
4204.868	2.594 ± 0.010	4.708 ± 0.037	4.763 ± 0.058
4205.842	2.598 ± 0.002	4.708 ± 0.015	4.734 ± 0.010
4207.852	2.595 ± 0.007	4.659 ± 0.017	4.846 ± 0.095
4213.878	2.616 ± 0.002	4.664 ± 0.016	4.648 ± 0.026
4217.855	2.593 ± 0.002	4.639 ± 0.029	4.762 ± 0.062
4228.821	2.579 ± 0.010	4.649 ± 0.037	4.606 ± 0.058
4230.786	2.577 ± 0.007	4.635 ± 0.008	4.762 ± 0.024
4233.874	2.581 ± 0.002	4.551 ± 0.031	4.751 ± 0.010
4234.899	2.560 ± 0.008	4.524 ± 0.014	4.849 ± 0.037
4235.883	2.570 ± 0.001	4.520 ± 0.014	4.746 ± 0.009
4238.873	2.567 ± 0.003	4.495 ± 0.023	4.760 ± 0.048
4239.931	2.567 ± 0.010	4.495 ± 0.037	4.686 ± 0.058
4240.885	2.555 ± 0.003	4.452 ± 0.000	4.692 ± 0.017
4241.921	2.571 ± 0.001	4.456 ± 0.014	4.623 ± 0.011
4316.657	2.500 ± 0.003	4.531 ± 0.015	4.760 ± 0.016
4329.820	2.572 ± 0.004	4.685 ± 0.030	4.471 ± 0.024
4333.532	2.584 ± 0.009	4.652 ± 0.006	4.573 ± 0.046
4338.544	2.578 ± 0.003	4.538 ± 0.033	4.898 ± 0.025
4342.652	2.575 ± 0.005	4.579 ± 0.034	4.789 ± 0.014
4347.534	2.589 ± 0.006	4.618 ± 0.002	4.677 ± 0.044
4353.537	2.569 ± 0.003	4.580 ± 0.022	4.800 ± 0.012
4354.725	2.604 ± 0.010	4.627 ± 0.037	4.490 ± 0.058
4358.491	2.577 ± 0.009	4.645 ± 0.001	4.623 ± 0.048
4363.503	2.567 ± 0.003	4.532 ± 0.020	4.707 ± 0.034
4369.601	2.524 ± 0.001	4.624 ± 0.011	4.804 ± 0.014
4371.497	2.537 ± 0.010	4.521 ± 0.037	4.739 ± 0.058
4377.514	2.535 ± 0.002	4.473 ± 0.009	4.735 ± 0.010
4385.550	2.526 ± 0.000	4.559 ± 0.019	4.728 ± 0.093
4393.508	2.540 ± 0.002	4.502 ± 0.009	4.696 ± 0.022
4408.527	2.549 ± 0.005	4.629 ± 0.017	4.649 ± 0.016

Table A1
(Continued)

HJD (days)	A = A1+A2 (mag)	B (mag)	C (mag)
4415.514	2.579 ± 0.007	4.635 ± 0.019	4.544 ± 0.055
4423.539	2.565 ± 0.008	4.669 ± 0.007	4.590 ± 0.026
4432.527	2.584 ± 0.003	4.718 ± 0.011	4.590 ± 0.021
4437.534	2.617 ± 0.014	4.641 ± 0.010	4.420 ± 0.006
4540.874	2.695 ± 0.006	4.773 ± 0.008	4.744 ± 0.035
4542.902	2.696 ± 0.010	4.791 ± 0.037	4.674 ± 0.058
4544.881	2.689 ± 0.007	4.771 ± 0.003	4.725 ± 0.006
4545.904	2.699 ± 0.013	4.779 ± 0.007	4.624 ± 0.079
4546.874	2.713 ± 0.007	4.810 ± 0.008	4.594 ± 0.026
4550.901	2.723 ± 0.004	4.749 ± 0.013	4.612 ± 0.029
4551.879	2.709 ± 0.010	4.801 ± 0.037	4.634 ± 0.058
4552.913	2.702 ± 0.010	4.725 ± 0.037	4.709 ± 0.058
4561.879	2.722 ± 0.005	4.812 ± 0.024	4.740 ± 0.029
4573.886	2.699 ± 0.010	4.800 ± 0.037	5.049 ± 0.058
4579.824	2.725 ± 0.010	4.619 ± 0.037	5.072 ± 0.058
4587.916	2.741 ± 0.010	4.721 ± 0.037	4.829 ± 0.058
4591.836	2.726 ± 0.000	4.739 ± 0.015	4.899 ± 0.015
4595.860	2.720 ± 0.006	4.726 ± 0.040	4.815 ± 0.059
4597.846	2.718 ± 0.003	4.695 ± 0.016	4.929 ± 0.012
4598.915	2.733 ± 0.010	4.626 ± 0.009	4.859 ± 0.041
4600.836	2.707 ± 0.010	4.669 ± 0.037	5.020 ± 0.058
4602.904	2.725 ± 0.010	4.633 ± 0.037	4.945 ± 0.058
4606.909	2.731 ± 0.001	4.609 ± 0.022	4.814 ± 0.016
4608.801	2.719 ± 0.001	4.697 ± 0.019	5.013 ± 0.041
4623.888	2.740 ± 0.001	4.663 ± 0.010	4.800 ± 0.007
4629.698	2.729 ± 0.001	4.792 ± 0.050	4.724 ± 0.063
4653.841	2.704 ± 0.003	4.703 ± 0.025	4.870 ± 0.028
4654.788	2.717 ± 0.004	4.689 ± 0.026	4.734 ± 0.012
4671.833	2.686 ± 0.006	4.768 ± 0.053	4.639 ± 0.077
4674.805	2.695 ± 0.000	4.663 ± 0.018	4.695 ± 0.009
4678.812	2.672 ± 0.004	4.696 ± 0.011	4.735 ± 0.054
4681.580	2.684 ± 0.004	4.668 ± 0.008	4.739 ± 0.007
4687.691	2.669 ± 0.002	4.589 ± 0.019	4.794 ± 0.026
4694.693	2.674 ± 0.005	4.666 ± 0.020	4.825 ± 0.041
4707.577	2.635 ± 0.008	4.536 ± 0.003	5.047 ± 0.067
4716.491	2.645 ± 0.010	4.621 ± 0.037	4.840 ± 0.058
4721.551	2.681 ± 0.008	4.558 ± 0.065	4.572 ± 0.012
4726.529	2.720 ± 0.008	4.420 ± 0.040	4.491 ± 0.022
4731.506	2.680 ± 0.002	4.544 ± 0.013	4.670 ± 0.047
4755.555	2.697 ± 0.002	4.522 ± 0.045	4.812 ± 0.010
4759.499	2.723 ± 0.018	4.526 ± 0.015	4.704 ± 0.083
4766.544	2.716 ± 0.002	4.592 ± 0.009	4.942 ± 0.011
4771.536	2.733 ± 0.010	4.662 ± 0.037	4.806 ± 0.058
4775.536	2.737 ± 0.004	4.612 ± 0.012	4.849 ± 0.023
4781.525	2.760 ± 0.003	4.505 ± 0.012	4.850 ± 0.015
4899.889	2.745 ± 0.003	4.734 ± 0.038	4.787 ± 0.007
4901.892	2.753 ± 0.010	4.844 ± 0.037	4.662 ± 0.058
4903.899	2.767 ± 0.005	4.721 ± 0.017	4.593 ± 0.060
4905.899	2.751 ± 0.003	4.728 ± 0.008	4.725 ± 0.014
4907.902	2.730 ± 0.000	4.764 ± 0.016	4.770 ± 0.027
4909.900	2.741 ± 0.008	4.749 ± 0.001	4.612 ± 0.052
4914.909	2.742 ± 0.004	4.732 ± 0.011	4.659 ± 0.018
4919.894	2.742 ± 0.011	4.748 ± 0.019	4.588 ± 0.054
4923.886	2.714 ± 0.010	4.725 ± 0.007	4.649 ± 0.044
4924.881	2.738 ± 0.008	4.704 ± 0.014	4.544 ± 0.034
4925.882	2.713 ± 0.003	4.735 ± 0.006	4.648 ± 0.012
4926.888	2.732 ± 0.000	4.719 ± 0.006	4.549 ± 0.043
4927.887	2.723 ± 0.008	4.742 ± 0.014	4.543 ± 0.018
4928.858	2.694 ± 0.013	4.730 ± 0.005	4.701 ± 0.010
4929.911	2.728 ± 0.007	4.665 ± 0.004	4.564 ± 0.037
4930.889	2.724 ± 0.011	4.699 ± 0.005	4.574 ± 0.023
4931.887	2.707 ± 0.006	4.683 ± 0.022	4.697 ± 0.025
4932.864	2.661 ± 0.003	4.784 ± 0.041	4.929 ± 0.010
4933.886	2.691 ± 0.002	4.656 ± 0.025	4.756 ± 0.010

Table A1
(Continued)

HJD (days)	A = A1+A2 (mag)	B (mag)	C (mag)
4934.886	2.707 ± 0.003	4.748 ± 0.014	4.644 ± 0.031
4935.889	2.715 ± 0.003	4.710 ± 0.008	4.563 ± 0.012
4940.841	2.705 ± 0.010	4.655 ± 0.017	4.635 ± 0.060
4950.837	2.702 ± 0.010	4.686 ± 0.037	4.649 ± 0.058
4955.855	2.700 ± 0.000	4.712 ± 0.001	4.716 ± 0.024
4961.818	2.695 ± 0.001	4.734 ± 0.017	4.724 ± 0.025
4966.870	2.712 ± 0.001	4.747 ± 0.000	4.764 ± 0.042
4972.850	2.718 ± 0.003	4.739 ± 0.034	4.787 ± 0.006
4976.800	2.762 ± 0.002	4.686 ± 0.027	4.788 ± 0.007
4982.752	2.750 ± 0.006	4.721 ± 0.001	4.789 ± 0.015
4984.851	2.728 ± 0.010	4.696 ± 0.037	4.926 ± 0.058
4992.802	2.767 ± 0.009	4.717 ± 0.037	4.718 ± 0.068
4998.715	2.762 ± 0.010	4.711 ± 0.037	4.801 ± 0.058
5004.849	2.761 ± 0.010	4.742 ± 0.037	4.737 ± 0.058
5008.833	2.750 ± 0.005	4.661 ± 0.000	4.901 ± 0.049
5012.763	2.753 ± 0.002	4.638 ± 0.016	4.847 ± 0.045
5014.790	2.750 ± 0.001	4.644 ± 0.013	4.842 ± 0.009
5015.742	2.735 ± 0.002	4.710 ± 0.010	4.892 ± 0.032
5016.847	2.742 ± 0.006	4.698 ± 0.029	4.889 ± 0.040
5017.911	2.741 ± 0.002	4.722 ± 0.036	4.846 ± 0.015
5018.841	2.745 ± 0.010	4.771 ± 0.037	4.744 ± 0.058
5019.854	2.745 ± 0.005	4.691 ± 0.014	4.925 ± 0.029
5020.821	2.748 ± 0.003	4.788 ± 0.024	4.800 ± 0.025
5021.839	2.745 ± 0.005	4.759 ± 0.016	4.801 ± 0.033
5022.863	2.755 ± 0.001	4.700 ± 0.023	4.811 ± 0.029
5023.891	2.748 ± 0.006	4.818 ± 0.020	4.740 ± 0.029
5024.866	2.737 ± 0.003	4.777 ± 0.022	4.776 ± 0.050
5042.577	2.777 ± 0.006	4.767 ± 0.041	4.663 ± 0.033
5047.630	2.753 ± 0.007	4.793 ± 0.038	4.850 ± 0.049
5053.628	2.747 ± 0.009	4.759 ± 0.096	4.752 ± 0.010
5057.527	2.752 ± 0.005	4.647 ± 0.021	4.746 ± 0.028
5063.553	2.721 ± 0.000	4.725 ± 0.011	4.803 ± 0.017
5067.509	2.728 ± 0.008	4.711 ± 0.002	4.718 ± 0.066
5072.535	2.722 ± 0.010	4.635 ± 0.037	4.745 ± 0.058
5082.500	2.677 ± 0.010	4.675 ± 0.037	4.746 ± 0.058
5098.599	2.636 ± 0.000	4.637 ± 0.016	4.811 ± 0.006
5104.573	2.626 ± 0.008	4.626 ± 0.010	4.702 ± 0.042
5107.492	2.636 ± 0.003	4.645 ± 0.001	4.648 ± 0.024
5111.500	2.628 ± 0.002	4.610 ± 0.032	4.800 ± 0.016
5115.514	2.617 ± 0.010	4.700 ± 0.037	4.801 ± 0.058
5120.569	2.639 ± 0.011	4.680 ± 0.016	4.722 ± 0.013
5121.505	2.662 ± 0.004	4.569 ± 0.038	4.763 ± 0.007
5123.502	2.651 ± 0.011	4.566 ± 0.022	4.806 ± 0.028
5127.519	2.701 ± 0.010	4.560 ± 0.037	4.654 ± 0.058
5131.509	2.677 ± 0.010	4.574 ± 0.037	4.731 ± 0.058
5273.899	2.572 ± 0.002	4.541 ± 0.009	4.634 ± 0.019
5275.903	2.579 ± 0.002	4.547 ± 0.012	4.522 ± 0.044
5278.899	2.559 ± 0.005	4.558 ± 0.009	4.636 ± 0.009
5281.891	2.565 ± 0.002	4.567 ± 0.004	4.641 ± 0.017
5283.878	2.574 ± 0.001	4.541 ± 0.011	4.597 ± 0.011
5284.881	2.573 ± 0.003	4.570 ± 0.105	4.610 ± 0.013
5285.880	2.559 ± 0.001	4.553 ± 0.003	4.639 ± 0.009
5291.869	2.538 ± 0.004	4.508 ± 0.014	4.567 ± 0.033
5295.886	2.524 ± 0.002	4.488 ± 0.018	4.601 ± 0.050
5300.865	2.523 ± 0.010	4.490 ± 0.037	4.527 ± 0.058
5304.866	2.530 ± 0.002	4.453 ± 0.011	4.518 ± 0.009
5308.861	2.508 ± 0.005	4.507 ± 0.012	4.557 ± 0.053
5313.868	2.500 ± 0.009	4.416 ± 0.040	4.556 ± 0.010
5317.828	2.490 ± 0.005	4.480 ± 0.034	4.479 ± 0.011
5321.875	2.479 ± 0.003	4.415 ± 0.026	4.615 ± 0.020
5324.883	2.462 ± 0.003	4.364 ± 0.007	4.701 ± 0.031
5328.854	2.458 ± 0.010	4.412 ± 0.050	4.674 ± 0.034
5335.783	2.459 ± 0.002	4.489 ± 0.008	4.490 ± 0.018
5336.738	2.464 ± 0.008	4.477 ± 0.014	4.469 ± 0.034

Table A1
(Continued)

HJD (days)	A = A1+A2 (mag)	B (mag)	C (mag)
5339.847	2.469 ± 0.004	4.411 ± 0.020	4.515 ± 0.009
5340.807	2.463 ± 0.004	4.426 ± 0.031	4.547 ± 0.009
5341.726	2.475 ± 0.000	4.485 ± 0.012	4.431 ± 0.013
5348.914	2.474 ± 0.010	4.362 ± 0.037	4.548 ± 0.058
5362.876	2.471 ± 0.001	4.375 ± 0.006	4.570 ± 0.011
5364.741	2.478 ± 0.000	4.425 ± 0.004	4.558 ± 0.015
5373.768	2.486 ± 0.003	4.381 ± 0.032	4.644 ± 0.016
5377.791	2.480 ± 0.006	4.378 ± 0.032	4.541 ± 0.009
5389.728	2.486 ± 0.004	4.408 ± 0.030	4.643 ± 0.025
5397.795	2.496 ± 0.003	4.373 ± 0.001	4.551 ± 0.005
5399.798	2.517 ± 0.006	4.393 ± 0.016	4.451 ± 0.024
5407.671	2.510 ± 0.010	4.438 ± 0.037	4.487 ± 0.058
5408.849	2.506 ± 0.003	4.478 ± 0.048	4.530 ± 0.017
5412.622	2.497 ± 0.001	4.377 ± 0.009	4.624 ± 0.020
5436.536	2.470 ± 0.007	4.419 ± 0.008	4.521 ± 0.037
5439.695	2.504 ± 0.003	4.397 ± 0.011	4.429 ± 0.022
5443.653	2.485 ± 0.001	4.434 ± 0.028	4.528 ± 0.032
5447.548	2.463 ± 0.002	4.425 ± 0.009	4.609 ± 0.007
5477.562	2.425 ± 0.006	4.425 ± 0.007	4.544 ± 0.028
5485.636	2.448 ± 0.002	4.481 ± 0.005	4.549 ± 0.004
5488.607	2.463 ± 0.002	4.473 ± 0.007	4.484 ± 0.022
5492.598	2.464 ± 0.006	4.463 ± 0.010	4.566 ± 0.032
5495.597	2.481 ± 0.002	4.465 ± 0.011	4.504 ± 0.024
5503.570	2.507 ± 0.003	4.462 ± 0.004	4.524 ± 0.016
5506.548	2.497 ± 0.005	4.465 ± 0.005	4.571 ± 0.022
5517.521	2.505 ± 0.009	4.461 ± 0.008	4.469 ± 0.047
5526.523	2.495 ± 0.003	4.474 ± 0.005	4.535 ± 0.022
5655.879	2.615 ± 0.007	4.534 ± 0.003	4.672 ± 0.004
5662.865	2.644 ± 0.006	4.574 ± 0.006	4.605 ± 0.022
5667.863	2.620 ± 0.008	4.569 ± 0.005	4.711 ± 0.040
5671.886	2.640 ± 0.004	4.547 ± 0.004	4.643 ± 0.029
5674.873	2.622 ± 0.002	4.572 ± 0.008	4.729 ± 0.017
5678.856	2.629 ± 0.005	4.552 ± 0.008	4.704 ± 0.025
5682.873	2.632 ± 0.003	4.545 ± 0.003	4.641 ± 0.017
5694.828	2.623 ± 0.005	4.537 ± 0.012	4.615 ± 0.012
5697.912	2.606 ± 0.004	4.559 ± 0.015	4.841 ± 0.025
5705.871	2.641 ± 0.007	4.500 ± 0.018	4.697 ± 0.008
5712.840	2.617 ± 0.001	4.530 ± 0.006	4.684 ± 0.003
5716.874	2.600 ± 0.004	4.562 ± 0.010	4.748 ± 0.022
5723.752	2.609 ± 0.003	4.580 ± 0.007	4.704 ± 0.045
5725.748	2.616 ± 0.002	4.564 ± 0.008	4.640 ± 0.017
5739.699	2.650 ± 0.016	4.534 ± 0.017	4.621 ± 0.025
5760.734	2.655 ± 0.002	4.433 ± 0.006	4.617 ± 0.059
5762.691	2.630 ± 0.008	4.530 ± 0.005	4.719 ± 0.005
5766.794	2.629 ± 0.002	4.558 ± 0.006	4.729 ± 0.021
5775.669	2.663 ± 0.012	4.540 ± 0.028	4.547 ± 0.062
5776.619	2.622 ± 0.001	4.579 ± 0.015	4.713 ± 0.009
5779.584	2.641 ± 0.006	4.564 ± 0.004	4.626 ± 0.045
5783.740	2.621 ± 0.003	4.576 ± 0.013	4.789 ± 0.007
5794.655	2.640 ± 0.002	4.586 ± 0.036	4.773 ± 0.009
5804.517	2.678 ± 0.007	4.632 ± 0.005	4.646 ± 0.029
5809.508	2.693 ± 0.005	4.631 ± 0.006	4.651 ± 0.024
5815.520	2.707 ± 0.008	4.622 ± 0.016	4.758 ± 0.020
5818.546	2.721 ± 0.008	4.602 ± 0.006	4.723 ± 0.004
5820.632	2.713 ± 0.004	4.614 ± 0.009	4.833 ± 0.005
5824.677	2.723 ± 0.004	4.631 ± 0.011	4.767 ± 0.014
5827.533	2.730 ± 0.004	4.578 ± 0.011	4.658 ± 0.008
5831.513	2.700 ± 0.004	4.637 ± 0.007	4.781 ± 0.021
5835.635	2.708 ± 0.007	4.657 ± 0.010	4.788 ± 0.022
5839.586	2.733 ± 0.006	4.587 ± 0.007	4.741 ± 0.024
5842.497	2.736 ± 0.002	4.627 ± 0.018	4.759 ± 0.006
5850.632	2.718 ± 0.007	4.643 ± 0.005	4.829 ± 0.017
5853.519	2.749 ± 0.003	4.601 ± 0.003	4.730 ± 0.029
5854.505	2.740 ± 0.002	4.588 ± 0.013	4.763 ± 0.010

Table A1
(Continued)

HJD (days)	A = A1+A2 (mag)	B (mag)	C (mag)
5861.506	2.745 ± 0.002	4.621 ± 0.012	4.831 ± 0.009
5869.511	2.719 ± 0.003	4.618 ± 0.005	4.779 ± 0.045
5873.550	2.721 ± 0.008	4.639 ± 0.013	4.706 ± 0.033
5882.516	2.721 ± 0.006	4.683 ± 0.004	4.694 ± 0.015
5885.518	2.708 ± 0.005	4.670 ± 0.021	4.756 ± 0.048
5892.528	2.713 ± 0.013	4.679 ± 0.021	4.853 ± 0.024
6023.881	2.795 ± 0.002	4.691 ± 0.008	4.710 ± 0.015
6028.875	2.777 ± 0.004	4.710 ± 0.011	4.852 ± 0.009
6029.884	2.762 ± 0.004	4.718 ± 0.012	4.918 ± 0.041
6047.845	2.770 ± 0.005	4.675 ± 0.008	4.702 ± 0.019
6050.839	2.768 ± 0.005	4.646 ± 0.010	4.753 ± 0.013
6053.868	2.764 ± 0.004	4.632 ± 0.025	4.730 ± 0.016
6062.898	2.756 ± 0.002	4.667 ± 0.012	4.956 ± 0.018
6070.911	2.759 ± 0.004	4.634 ± 0.010	4.931 ± 0.008
6092.913	2.765 ± 0.005	4.672 ± 0.021	4.867 ± 0.004
6094.868	2.776 ± 0.001	4.666 ± 0.006	4.863 ± 0.008
6098.874	2.750 ± 0.006	4.696 ± 0.016	4.961 ± 0.026
6105.713	2.745 ± 0.001	4.688 ± 0.006	4.862 ± 0.017
6109.796	2.763 ± 0.007	4.711 ± 0.006	4.875 ± 0.010
6118.711	2.764 ± 0.001	4.695 ± 0.011	4.893 ± 0.004
6129.679	2.791 ± 0.005	4.702 ± 0.018	4.860 ± 0.034
6133.625	2.809 ± 0.002	4.727 ± 0.008	4.823 ± 0.024
6138.566	2.824 ± 0.010	4.773 ± 0.009	4.761 ± 0.016
6147.576	2.841 ± 0.009	4.770 ± 0.010	4.886 ± 0.009
6151.567	2.837 ± 0.012	4.712 ± 0.009	4.960 ± 0.007
6165.542	2.811 ± 0.003	4.807 ± 0.010	5.096 ± 0.014
6168.561	2.835 ± 0.006	4.739 ± 0.005	4.982 ± 0.035
6169.549	2.849 ± 0.002	4.735 ± 0.008	4.899 ± 0.017
6173.659	2.837 ± 0.003	4.771 ± 0.016	4.989 ± 0.008
6175.697	2.849 ± 0.002	4.762 ± 0.004	4.948 ± 0.011
6181.562	2.857 ± 0.005	4.700 ± 0.012	4.914 ± 0.004
6185.489	2.844 ± 0.007	4.731 ± 0.004	4.905 ± 0.024
6190.504	2.836 ± 0.005	4.730 ± 0.006	4.960 ± 0.024
6193.493	2.846 ± 0.006	4.690 ± 0.010	4.824 ± 0.028
6197.523	2.822 ± 0.002	4.719 ± 0.006	4.973 ± 0.017
6205.496	2.822 ± 0.011	4.739 ± 0.012	4.914 ± 0.027
6209.490	2.819 ± 0.002	4.739 ± 0.052	5.004 ± 0.038
6210.499	2.813 ± 0.007	4.759 ± 0.017	5.012 ± 0.007
6213.520	2.835 ± 0.013	4.761 ± 0.011	4.814 ± 0.090
6217.591	2.823 ± 0.002	4.812 ± 0.003	4.978 ± 0.034
6221.511	2.838 ± 0.010	4.775 ± 0.009	4.953 ± 0.022
6224.531	2.839 ± 0.002	4.830 ± 0.014	4.948 ± 0.006
6225.521	2.842 ± 0.006	4.781 ± 0.021	5.048 ± 0.040
6229.510	2.844 ± 0.012	4.787 ± 0.006	5.042 ± 0.064
6236.528	2.854 ± 0.002	4.827 ± 0.004	5.072 ± 0.009
6390.900	2.785 ± 0.004	4.709 ± 0.007	4.795 ± 0.015
6395.912	2.788 ± 0.004	4.691 ± 0.010	4.819 ± 0.027
6401.892	2.798 ± 0.007	4.726 ± 0.003	4.840 ± 0.020
6405.873	2.763 ± 0.006	4.767 ± 0.012	5.028 ± 0.041
6409.863	2.840 ± 0.008	4.702 ± 0.019	4.713 ± 0.031
6431.850	2.804 ± 0.004	4.777 ± 0.026	5.002 ± 0.014
6435.851	2.824 ± 0.002	4.708 ± 0.025	4.846 ± 0.020
6441.787	2.819 ± 0.004	4.745 ± 0.024	4.898 ± 0.075
6443.755	2.816 ± 0.004	4.736 ± 0.007	4.746 ± 0.033
6447.734	2.823 ± 0.008	4.788 ± 0.005	4.789 ± 0.014
6455.875	2.834 ± 0.002	4.733 ± 0.014	4.949 ± 0.028
6460.668	2.838 ± 0.005	4.781 ± 0.026	4.871 ± 0.027
6468.705	2.836 ± 0.009	4.741 ± 0.005	4.896 ± 0.014
6472.782	2.835 ± 0.009	4.718 ± 0.024	4.940 ± 0.022
6476.891	2.828 ± 0.007	4.766 ± 0.007	5.002 ± 0.064
6483.897	2.846 ± 0.011	4.817 ± 0.025	4.889 ± 0.040
6487.851	2.799 ± 0.001	4.731 ± 0.003	4.874 ± 0.006
6496.683	2.791 ± 0.006	4.754 ± 0.020	4.890 ± 0.023
6504.781	2.770 ± 0.006	4.826 ± 0.012	4.948 ± 0.081

Table A1
(Continued)

HJD (days)	A = A1+A2 (mag)	B (mag)	C (mag)
6507.731	2.803 ± 0.001	4.712 ± 0.032	4.875 ± 0.041
6519.649	2.805 ± 0.004	4.702 ± 0.020	4.936 ± 0.011
6529.605	2.802 ± 0.004	4.749 ± 0.011	5.036 ± 0.021
6532.641	2.797 ± 0.003	4.734 ± 0.004	4.933 ± 0.016
6536.570	2.813 ± 0.001	4.704 ± 0.017	4.913 ± 0.025
6544.550	2.837 ± 0.002	4.741 ± 0.004	4.847 ± 0.032
6548.698	2.813 ± 0.003	4.747 ± 0.008	4.923 ± 0.019
6552.500	2.804 ± 0.002	4.738 ± 0.032	4.970 ± 0.072
6556.492	2.843 ± 0.008	4.733 ± 0.006	4.785 ± 0.078
6569.497	2.797 ± 0.003	4.731 ± 0.007	4.834 ± 0.005
6576.500	2.805 ± 0.001	4.691 ± 0.022	4.907 ± 0.004
6580.507	2.790 ± 0.005	4.727 ± 0.014	4.948 ± 0.020
6581.581	2.805 ± 0.002	4.743 ± 0.014	4.876 ± 0.016
6584.605	2.810 ± 0.002	4.750 ± 0.005	4.890 ± 0.023
6592.565	2.829 ± 0.003	4.782 ± 0.016	4.911 ± 0.026
6604.514	2.858 ± 0.003	4.763 ± 0.007	4.849 ± 0.014
6609.516	2.842 ± 0.004	4.742 ± 0.006	4.995 ± 0.016
6765.887	3.037 ± 0.011	4.902 ± 0.016	4.907 ± 0.054
6775.875	3.021 ± 0.002	4.862 ± 0.003	4.888 ± 0.013
6781.830	2.983 ± 0.004	4.866 ± 0.020	5.009 ± 0.025
6789.876	2.964 ± 0.001	4.803 ± 0.011	5.095 ± 0.031
6805.808	2.914 ± 0.002	4.787 ± 0.003	4.995 ± 0.018
6814.872	2.874 ± 0.001	4.734 ± 0.031	5.049 ± 0.014
6822.683	2.872 ± 0.004	4.811 ± 0.011	4.890 ± 0.014
6834.718	2.899 ± 0.005	4.804 ± 0.006	4.817 ± 0.022
6846.801	2.888 ± 0.005	4.733 ± 0.012	4.986 ± 0.009
6863.610	2.926 ± 0.007	4.830 ± 0.004	4.730 ± 0.044
6870.693	2.899 ± 0.005	4.820 ± 0.018	5.022 ± 0.014
6878.565	2.935 ± 0.002	4.858 ± 0.012	4.831 ± 0.022
6884.734	2.917 ± 0.004	4.787 ± 0.011	5.007 ± 0.028
6896.518	2.919 ± 0.002	4.871 ± 0.009	4.943 ± 0.008
6900.488	2.971 ± 0.004	4.813 ± 0.008	4.791 ± 0.015
6904.534	2.956 ± 0.002	4.842 ± 0.013	4.872 ± 0.014
6908.504	2.941 ± 0.005	4.845 ± 0.014	4.930 ± 0.007
6930.565	2.953 ± 0.002	4.830 ± 0.016	5.060 ± 0.011
6947.502	2.975 ± 0.004	4.811 ± 0.032	5.046 ± 0.008
6950.585	2.979 ± 0.001	4.909 ± 0.004	4.994 ± 0.016
6959.512	2.981 ± 0.008	4.951 ± 0.006	5.116 ± 0.028
6963.563	2.995 ± 0.012	4.947 ± 0.028	5.005 ± 0.062
6966.522	2.966 ± 0.012	4.962 ± 0.008	5.238 ± 0.056
6973.545	2.992 ± 0.010	4.945 ± 0.011	5.095 ± 0.042
6974.552	2.990 ± 0.003	4.945 ± 0.004	5.143 ± 0.011
6982.526	3.002 ± 0.012	4.968 ± 0.009	5.110 ± 0.064
7113.879	3.062 ± 0.006	4.993 ± 0.016	5.105 ± 0.033
7116.908	3.039 ± 0.002	4.988 ± 0.024	5.139 ± 0.009
7123.885	3.062 ± 0.003	5.004 ± 0.008	5.025 ± 0.016
7130.875	3.067 ± 0.011	5.018 ± 0.010	5.011 ± 0.069
7138.834	3.073 ± 0.008	5.040 ± 0.010	5.122 ± 0.023
7141.829	3.087 ± 0.003	5.036 ± 0.012	5.003 ± 0.018
7145.820	3.109 ± 0.007	5.024 ± 0.012	5.004 ± 0.035
7150.778	3.131 ± 0.005	5.018 ± 0.015	4.957 ± 0.026
7157.864	3.114 ± 0.006	4.983 ± 0.008	5.130 ± 0.031
7170.786	3.113 ± 0.002	5.081 ± 0.008	5.244 ± 0.018
7189.885	3.140 ± 0.002	5.042 ± 0.007	5.218 ± 0.009
7196.852	3.159 ± 0.006	4.991 ± 0.006	5.203 ± 0.022
7200.704	3.154 ± 0.005	5.018 ± 0.010	5.151 ± 0.027
7209.809	3.136 ± 0.010	5.032 ± 0.035	5.301 ± 0.067
7219.687	3.141 ± 0.012	4.985 ± 0.028	5.127 ± 0.062
7223.757	3.102 ± 0.001	5.006 ± 0.017	5.320 ± 0.041
7227.582	3.115 ± 0.004	4.984 ± 0.006	5.127 ± 0.023
7235.725	3.079 ± 0.005	4.911 ± 0.021	5.271 ± 0.025
7252.566	3.048 ± 0.001	4.952 ± 0.007	5.099 ± 0.008
7258.541	3.032 ± 0.002	4.957 ± 0.007	5.103 ± 0.005
7263.541	3.026 ± 0.013	5.003 ± 0.008	5.130 ± 0.112

Table A1
(Continued)

HJD (days)	A = A1+A2 (mag)	B (mag)	C (mag)
7267.506	3.026 ± 0.002	4.969 ± 0.007	5.141 ± 0.004
7270.514	3.038 ± 0.002	4.939 ± 0.007	5.079 ± 0.009
7274.503	3.050 ± 0.010	4.949 ± 0.011	5.003 ± 0.024
7278.498	3.026 ± 0.001	4.939 ± 0.009	5.141 ± 0.017
7287.508	3.018 ± 0.010	4.944 ± 0.005	5.219 ± 0.066
7293.605	3.021 ± 0.001	4.910 ± 0.009	5.146 ± 0.004
7297.540	3.004 ± 0.002	4.889 ± 0.008	5.220 ± 0.007
7301.526	2.997 ± 0.009	4.869 ± 0.017	5.179 ± 0.013
7311.590	2.993 ± 0.002	4.912 ± 0.009	5.107 ± 0.021
7324.572	2.988 ± 0.006	4.913 ± 0.006	5.040 ± 0.015
7475.879	2.894 ± 0.008	4.849 ± 0.006	4.924 ± 0.025
7486.892	2.967 ± 0.023	4.884 ± 0.018	4.950 ± 0.045
7495.869	2.929 ± 0.008	4.844 ± 0.004	5.015 ± 0.048
7499.826	2.965 ± 0.013	4.878 ± 0.029	4.900 ± 0.016
7511.873	2.932 ± 0.005	4.856 ± 0.018	4.879 ± 0.033
7528.927	2.952 ± 0.003	4.833 ± 0.004	5.015 ± 0.053
7536.912	2.932 ± 0.003	4.827 ± 0.010	5.062 ± 0.040
7566.845	2.941 ± 0.002	4.855 ± 0.010	4.947 ± 0.020
7579.665	2.914 ± 0.018	4.828 ± 0.014	4.897 ± 0.092
7590.653	2.919 ± 0.003	4.860 ± 0.006	4.849 ± 0.027
7593.579	2.933 ± 0.008	4.872 ± 0.006	4.839 ± 0.056
7605.624	2.933 ± 0.002	4.817 ± 0.004	4.928 ± 0.015
7609.533	2.941 ± 0.003	4.866 ± 0.006	4.875 ± 0.044
7622.650	2.905 ± 0.002	4.863 ± 0.017	5.100 ± 0.006
7624.548	2.918 ± 0.004	4.890 ± 0.007	4.963 ± 0.057
7629.631	2.919 ± 0.004	4.869 ± 0.061	5.076 ± 0.010
7632.655	2.925 ± 0.004	4.843 ± 0.014	5.047 ± 0.010
7636.513	2.870 ± 0.011	4.960 ± 0.030	5.253 ± 0.096
7651.659	2.944 ± 0.004	4.878 ± 0.006	5.073 ± 0.006
7655.597	2.935 ± 0.001	4.860 ± 0.012	5.065 ± 0.012
7663.573	2.950 ± 0.003	4.849 ± 0.009	5.077 ± 0.012
7671.557	2.970 ± 0.007	4.863 ± 0.004	5.051 ± 0.029
7683.507	2.916 ± 0.010	4.979 ± 0.015	5.346 ± 0.098
7687.509	2.962 ± 0.001	4.837 ± 0.012	5.126 ± 0.016
7696.513	2.961 ± 0.005	4.865 ± 0.003	5.078 ± 0.011
7717.551	2.986 ± 0.005	4.973 ± 0.009	4.934 ± 0.020

Note. The heliocentric julian date (HJD) given is HJD-2,450,000 days. Images A = A1+A2, B, and C are given in magnitudes relative to the nearby reference stars.

ORCID iDs

Matthew A. Cornachione https://orcid.org/0000-0003-1012-4771
Christopher W. Morgan https://orcid.org/0000-0003-2460-9999
Misty C. Bentz https://orcid.org/0000-0002-2816-5398
Vivien Bonvin https://orcid.org/0000-0003-1471-3952
Emilio E. Falco https://orcid.org/0000-0002-7061-6519

References

Antonucci, R. 1993, ARA&A, 31, 473
Bate, N. F., Floyd, D. J. E., Webster, R. L., & Wyithe, J. S. B. 2008, MNRAS, 391, 1955
Bate, N. F., Vernardos, G., O'Dowd, M. J., et al. 2018, MNRAS, 479, 4796
Bentz, M. C., Walsh, J. L., Barth, A. J., et al. 2010, ApJ, 716, 993
Blackburne, J. A., Kochanek, C. S., Chen, B., Dai, X., & Chartas, G. 2014, ApJ, 789, 125
Blackburne, J. A., Pooley, D., Rappaport, S., & Schechter, P. L. 2011, ApJ, 729, 34
Bonning, E. W., Cheng, L., Shields, G. A., Salviander, S., & Gebhardt, K. 2007, ApJ, 659, 211
Bonvin, V., Chan, J. H. H., Millon, M., et al. 2018, A&A, 616, A183
Bonvin, V., Tewes, M., Courbin, F., et al. 2016, A&A, 585, A88
Cackett, E. M., Chiang, C.-Y., McHardy, I., et al. 2018, ApJ, 857, 53
Cackett, E. M., Horne, K., & Winkler, H. 2007, MNRAS, 380, 669
Chang, K., & Refsdal, S. 1979, Natur, 282, 561
Chantry, V., Sluse, D., & Magain, P. 2010, A&A, 522, A95
Courbin, F., Eigenbrod, A., Vuissoz, C., Meylan, G., & Magain, P. 2005, in IAU Symp. 225, Gravitational Lensing Impact on Cosmology, ed. Y. Mellier & G. Meylan (Cambridge: Cambridge Univ. Press), 297
Dai, X., Kochanek, C. S., Chartas, G., et al. 2010, ApJ, 709, 278
Denney, K. D., Pogge, R. W., Assef, R. J., et al. 2013, ApJ, 775, 60
Edelson, R., Gelbord, J. M., Horne, K., et al. 2015, ApJ, 806, 129
Gaskell, C. M. 2008, RMxAC, 32, 1
Hainline, L. J., Morgan, C. W., Beach, J. N., et al. 2012, ApJ, 744, 104
Hainline, L. J., Morgan, C. W., MacLeod, C. L., et al. 2013, ApJ, 774, 69
Hall, P. B., Sarrouh, G. T., & Horne, K. 2018, ApJ, 854, 93
Jiménez-Vicente, J., Mediavilla, E., Muñoz, J. A., & Kochanek, C. S. 2012, ApJ, 751, 106
Keeton, C. R. 2001, arXiv:astro-ph/0102340
Kelly, B. C., Bechtold, J., & Siemiginowska, A. 2009, ApJ, 698, 895
Kochanek, C. S. 2004, ApJ, 605, 58
Kochanek, C. S., Falco, E. E., Impey, C. D., et al. 1999, in AIP Conf. Ser. 470, After the Dark Ages: When Galaxies were Young (the Universe at $2 < Z < 5$), ed. S. Holt & E. Smith (Melville, NY: AIP), 163
Kochanek, C. S., Morgan, N. D., Falco, E. E., et al. 2006, ApJ, 640, 47
Lehár, J., Falco, E. E., Kochanek, C. S., et al. 2000, ApJ, 536, 584
Liao, K., Treu, T., Marshall, P., et al. 2015, ApJ, 800, 11
MacLeod, C. L., Ivezić, Ž., Kochanek, C. S., et al. 2010, ApJ, 721, 1014
MacLeod, C. L., Morgan, C. W., Mosquera, A., et al. 2015, ApJ, 806, 258
Magain, P., Courbin, F., Gillon, M., et al. 2007, A&A, 461, 373
Magain, P., Courbin, F., & Sohy, S. 1998, ApJ, 494, 472
Mediavilla, E., Muñoz, J. A., Kochanek, C. S., et al. 2011, ApJ, 730, 16
Morgan, C. W., Hainline, L. J., Chen, B., et al. 2012, ApJ, 756, 52
Morgan, C. W., Hyer, G. E., Bonvin, V., et al. 2018, ApJ, 869, 106
Morgan, C. W., Kochanek, C. S., Dai, X., Morgan, N. D., & Falco, E. E. 2008, ApJ, 689, 755
Morgan, C. W., Kochanek, C. S., Morgan, N. D., & Falco, E. E. 2006, ApJ, 647, 874
Morgan, C. W., Kochanek, C. S., Morgan, N. D., & Falco, E. E. 2010, ApJ, 712, 1129
Morgan, N. D., Caldwell, J. A. R., Schechter, P. L., et al. 2004, AJ, 127, 2617
Mortonson, M. J., Schechter, P. L., & Wambsganss, J. 2005, ApJ, 628, 594
Mosquera, A. M., & Kochanek, C. S. 2011, ApJ, 738, 96
Mosquera, A. M., Kochanek, C. S., Chen, B., et al. 2013, ApJ, 769, 53
Mosquera, A. M., Muñoz, J. A., Mediavilla, E., & Kochanek, C. S. 2011, ApJ, 728, 145
Motta, V., Mediavilla, E., Rojas, K., et al. 2017, ApJ, 835, 132
Muñoz, J. A., Falco, E. E., Kochanek, C. S., et al. 1998, Ap&SS, 263, 51
Navarro, J. F., Frenk, C. S., & White, S. D. M. 1997, ApJ, 490, 493
Ofek, E. O., Rix, H.-W., & Maoz, D. 2003, MNRAS, 343, 639
Park, D., Woo, J.-H., Denney, K. D., & Shin, J. 2013, ApJ, 770, 87
Peterson, B. M., Ferrarese, L., Gilbert, K. M., et al. 2004, ApJ, 613, 682
Poindexter, S., Morgan, N., Kochanek, C. S., & Falco, E. E. 2007, ApJ, 660, 146
Pooley, D., Blackburne, J. A., Rappaport, S., & Schechter, P. L. 2007, ApJ, 661, 19
Pooley, D., Rappaport, S., Blackburne, J. A., Schechter, P. L., & Wambsganss, J. 2012, ApJ, 744, 111
Schechter, P. L., Pooley, D., Blackburne, J. A., & Wambsganss, J. 2014, ApJ, 793, 96
Sergeev, S. G., Doroshenko, V. T., Golubinskiy, Y. V., Merkulova, N. I., & Sergeeva, E. A. 2005, ApJ, 622, 129
Sluse, D., Chantry, V., Magain, P., Courbin, F., & Meylan, G. 2012, A&A, 538, A99
Sun, W.-H., & Malkan, M. A. 1989, ApJ, 346, 68
Tewes, M., Courbin, F., & Meylan, G. 2013, A&A, 553, A120
Urry, C. M., & Padovani, P. 1995, PASP, 107, 803
Vanden Berk, D. E., Wilhite, B. C., Kron, R. G., et al. 2004, ApJ, 601, 692
Vernardos, G., & Tsagkatakis, G. 2019, MNRAS, 486, 1944
Véron-Cetty, M. P., & Véron, P. 2010, A&A, 518, A10
Vestergaard, M., & Peterson, B. M. 2006, ApJ, 641, 689
Vuissoz, C., Courbin, F., Sluse, D., et al. 2007, A&A, 464, 845
Vuissoz, C., Courbin, F., Sluse, D., et al. 2008, A&A, 488, 481
Wills, B. J., & Brotherton, M. S. 1995, ApJL, 448, L81